Annealing Cryogenically Irradiated High Temperature Superconductors with Current Pulses

by

Zoe Lilah Fisher

Submitted to the Department of Nuclear Science and Engineering
in partial fulfillment of the requirements for the degree of

Masters of Science in Nuclear Science and Engineering

at the

MASSACHUSETTS INSTITUTE OF TECHNOLOGY

June 2023

Authored by: Zoe Lilah Fisher
Department of Nuclear Science and Engineering
May 15, 2023

Certified by: Dennis G. Whyte
Director, Plasma Science and Fusion Center
Hitachi America Professor of Engineering
Thesis Supervisor

Certified by: Michael P. Short
Associate Director, Plasma Science and Fusion Center
Class of '42 Associate Professor of Nuclear Science and Engineering
Thesis Supervisor

Accepted by: Ju Li
Battelle Energy Alliance Professor of Nuclear Science and Engineering
and Professor of Materials Science and Engineering
Chairman, Department Committee on Graduate Theses

Annealing Cryogenically Irradiated High Temperature Superconductors with Current Pulses

by

Zoe Lilah Fisher

Submitted to the Department of Nuclear Science and Engineering
on May 15, 2023, in partial fulfillment of the
requirements for the degree of
Masters of Science in Nuclear Science and Engineering

Abstract

Tokamak fusion power plants rely on electrogmanets engineered from high temperature superconductors (HTS) made of Rare Earth Barium Copper Oxide (REBCO) to confine a thermonuclear grade plasma. The HTS performance must be predictable despite the radiation damage caused by fast neutrons from fusion reactions that damage to the REBCO microstructure, decreasing the magnet's critical current. This lowers the reactor's achievable magnetic field–and therefore performance. The damage, however, is not necessarily permanent. By applying a short current pulse above the critical current of the coated conductor, resistive heating briefly raises the REBCO's temperature well above that of the surrounding cryogenic environment. This process, called annealing, heals defects and recovers some of the performance losses. Magnets are the limiting factor for tokamak lifetimes, therefore pulse annealing could dramatically increase the economical viability of fusion energy by reducing shutdown frequency and duration.

This experiment focuses on sending 400 A pulses through an irradiated HTS tape to identify the optimal duration for critical current recovery. Using a cryogenic proton irradiation facility capable of applying current pulses as high as 2000 A and as short as 100 ns, we found that a 400 A pulse can display up to 400% critical current recovery as defined by the difference between the post-irradiation and post-annealing values. The optimal length for this current pulse is 5.5 ms, which results in a maximum calculated temperature of 630 K in the REBCO microstructure. Future works will pursue measuring (rather than calculating) the temperature in the REBCO microstructure and parameterizing the maximum critical current recovery at different pulse amplitudes.

Thesis Supervisor: Dennis G. Whyte
Title: Director, Plasma Science and Fusion Center
Hitachi America Professor of Engineering

Thesis Supervisor: Michael P. Short
Title: Associate Director, Plasma Science and Fusion Center
Class of '42 Associate Professor of Nuclear Science and Engineering

Acknowledgments

In (mostly) loving memory of DANTE.

To Professor Dennis Whyte, thank you for giving me the opportunity to pursue fusion research. To Professor Michael Short, thank you for introducing me to the world of Nuclear Science, and for your heartfelt willingness to help me through countless hurdles. To Professor Zachary Hartwig, thank you for guiding me to and through the Vault, even when I am not actually one of your students.

I owe an insurmountable amount of gratitude to Dr. David Fischer. You may misspell your last name, but you have offered me an endless supply of patience and mentorship over the years. Any accelerator run would have been impossible without Dr. Kevin Woller's expertise and incomplete without his wry humor. I would be remiss if I did not mention Alexis Devitre and his persistent help. I usually appreciate it, and I am apologizing right now for when I do not. Thank you for offering it regardless.

For putting up with me and my never-ending questions (about both coursework and life decisions), I would like to thank Brandy Baker. Heather Barry does not like very sappy things, so I will simply state that my absolute favorite days of the week are Mondays, Wednesdays, and Fridays.

To my parents, Ian and Gayle, thank you for gifting me wonder, curiosity, and just-a-little-too-much argumentativeness. To my sisters, Gia and Ava, thank you for the constant influx of terrible viral videos to distract me from writing this thesis. I love you.

Contents

List of Figures

List of Tables

Chapter 1

Introduction

Although the development of fusion energy is a fascinating test of modern physics, it serves a greater importance: decarbonization. Global warming's looming presence is the powerful motivator for the SPARC tokamak, a fusion reactor Commonwealth Fusion Systems (CFS) is currently constructing with the help of MIT's Plasma Science and Fusion Center (PSFC). The tokamak, often referred to as a "star in a bottle," is free of fossil fuels and shines an optimistic light on the currently bleak future of climate change. As the National Aeronautics and Space Administration plainly states, "the effects of human-caused global warming are happening now, are irreversible for people alive today, and will worsen as long as humans add greenhouse gasses to the atmosphere" [24].

SPARC offers a higher power density than the sun by housing a thermonuclear grade plasma. However, this plasma requires a refined magnetic confinement system. The fusion reactor's performance scales with the magnitude of the magnetic field to the fourth power. Therefore, achieving higher magnetic fields means a dramatic increase in fusion power. SPARC relies on electromagnets engineered from high temperature superconductors (HTS) made with Rare Earth Barium Copper Oxide (REBCO), a material discovered to be superconducting in 1986 [25]. These superconductors can produce magnetic fields past 20 T, enabling substantially smaller fusion devices than previously blueprinted.

Inevitably, the REBCO tapes installed in SPARC are subject to neutron irradia-

tion, which creates defects in the REBCO microstructure [26]. At high damage levels, these irradiated HTS tapes lose performance. This limits the lifetimes of commercial fusion devices, such as the follow-up device to SPARC, ARC. The performance of an HTS tape is often gauged through the critical current, or the current at which a superconductor experiences the onset of the resistive regime. Damaged HTS tapes exhibit a decreased critical current—when exposed to enough proton bombardment in the laboratory, they display 100% degradation.

Previous studies prove that heat treatment can partially revert these defects [27]. This process is called annealing, and takes place when the temperature of a sample is raised until the quantity of defects decreases. Until now, HTS annealing experiments have involved raising the environment's temperature for extended periods of time (on the order of hours) [28]. This is not practical for use inside of a working reactor; increasing an entire tokamak's temperature for sustained periods of time would disrupt energy production and require either inserting excessive amounts of heat or temporarily deconstructing the magnets to heat them individually. This work proposes a method by which HTS tapes can be annealed from heating within the tapes on the sub-second scale while the majority of the magnet structure remains cool. Applied in a tokamak, this process could heal damaged magnets without incurring downtime.

This thesis focuses on using current pulses—and the heating power generated within the HTS tape by these pulses—to heal REBCO damaged from proton irradiation. By sending a current pulse above the post-irradiation critical current value of an HTS tape, the damaged REBCO will experience a resistance [29]. The energy transferred to the tape during the pulse heats the tape, annealing defects in the REBCO microstructure, and increasing the critical current value. Figure 1-1 illustrates how the current-voltage curve of the HTS tape changes throughout this experiment.

This work explores the impact of the pulse duration. Short-term ohmic heating proves a possible HTS annealing method. Provided that the magnetic coil has minimal inductance during a current pulse, this method could efficiently anneal damaged HTS inside SPARC and other future tokamaks. Furthermore, this discovery reveals valuable information regarding the thermal and time variables necessary to recover

HTS performance.

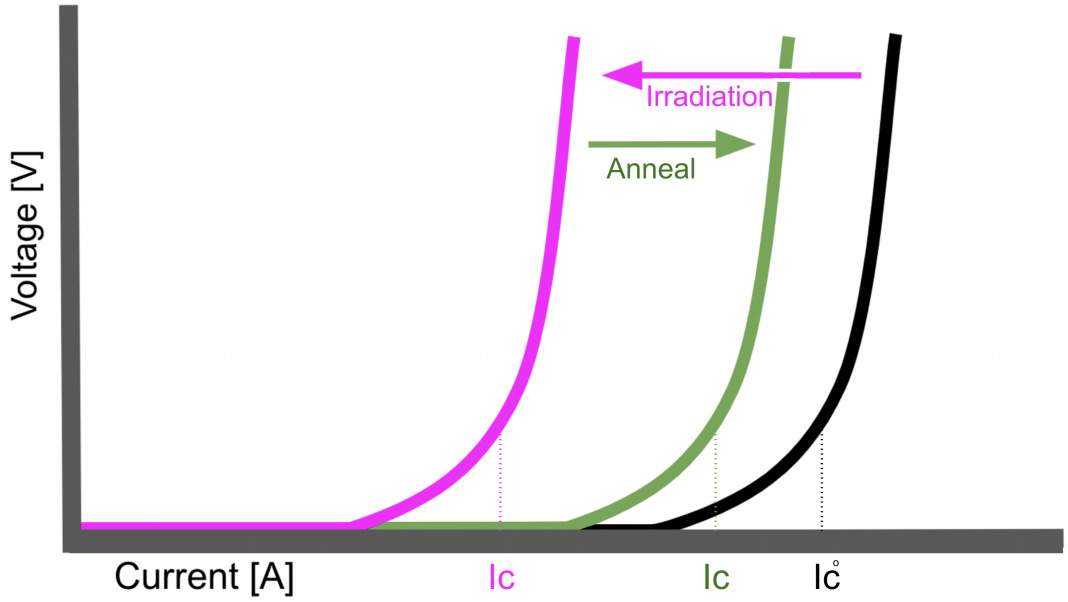

Figure 1-1: A conceptual image showing how an HTS tape's critical current will decrease after irradiation and increase after this annealing experiment. While not to scale, this image still displays how an annealed tape will exhibit a higher critical current than immediately post irradiation, but still a lower critical current than the pristine tape.

Chapter 2

Background

2.1 Tokamaks

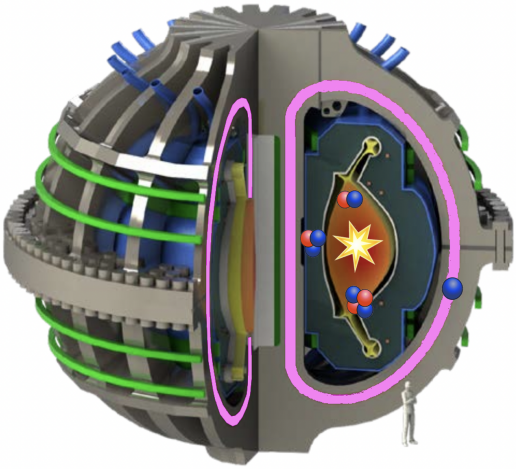

Figure 2-1: The conceptual design for the ARC reactor [1]. The plasma reaction is drawn as a cartoon inside the vacuum vessel with fast neutrons ($> 100\,\text{keV}$) travelling towards the toroidal field magnet.

Tokamaks are toroidal fusion reactors. As seen in Figures 2-1 and 2-2, the plasma is isolated by a vacuum vessel and confined by toroidal field magnets. Its shape is moderated by the poloidal magnets. The magnetic confinement, however, does not prevent radiation from escaping the plasma because neutrons are not charged. Therefore, a neutron blanket functions as both magnet/environment protection and

tritium breeding. Still, the neutron blanket does not protect the magnets from all neutron degradation [30]. Tokamak design studies generally expect a lifetime fluence of 3×10^{18} particles/cm^2 [31, 32, 8].

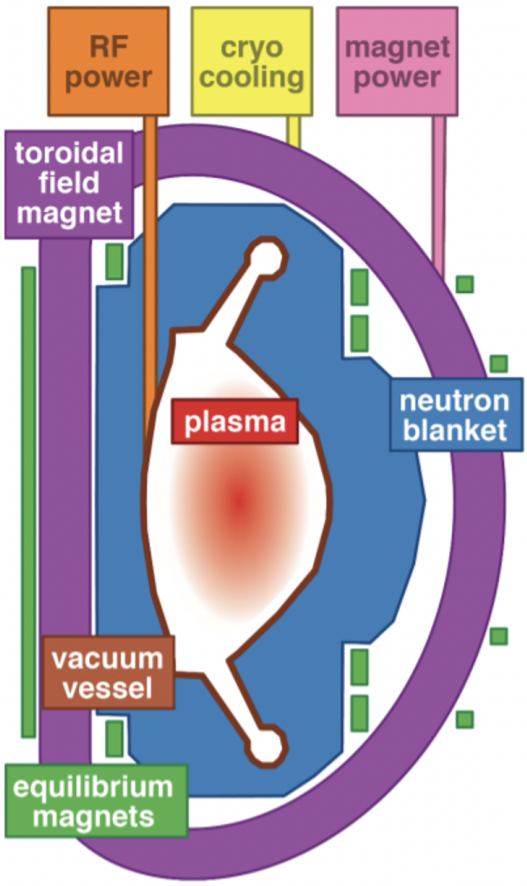

Figure 2-2: The radial cross section of a tokamak. The toroidal feild magnets provide the confining field for the plasma, while the equilibrium (or poloidal) magnets control the plasma's shape and position. The vacuum vessel keeps the plasma from the outside environment. The neutron blanket protects the magnets by absorbing neutrons (which allows it to breed tritium for more fusion reactions) [2].

SPARC uses deuterium and tritium as fuel. They combine into a plasma, which produces helium, neutrons, and—most importantly—energy (17.6 MeV in total) [2]:

$$D + T \quad \rightarrow \quad {}^4He + n. \tag{2.1}$$

The neutron exits the reaction with 14.1 MeV and the helium particle with 3.5 MeV. As previously mentioned, some high energy fusion neutrons escape the neutron blanket and may interact with the superconducting magnets [33].

2.2 Superconductivity

Superconductivity is defined by the presence of Cooper pairs, electrons with identical speeds but opposite spins and directions. The energy of the pairing interaction in Cooper pairs is extremely weak, ergo they only remain bound under a very low temperature called the transition (or critical) temperature T_c [34]. The two forms of superconductors are called type I and type II. Type I superconductors lose their superconductiviting properties at high magnetic field and are therefore not suited for strong electromagnets [35]. Type II superconductors, like REBCO, are ideal electromagnets [30]. This background will focus on type II superconductivity.

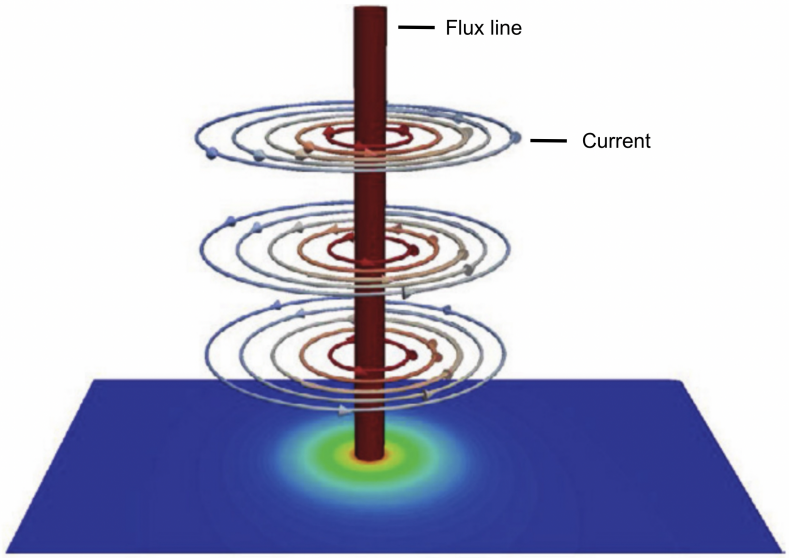

Figure 2-3: A simulation of the currents surrounding a single flux line from [3] with added labels.

Vortices, or flux lines, are regular cylindrical structures with a radius ξ (the coherence length) and are surrounded by superconducting shielding currents with a radius λ (the penetration depth). Figure 2-3 shows a flux line entering the material, which is normal conducting, as well as the superconducting shielding currents that surround the flux line. Each flux line has exactly one flux quantum Φ_0, a constant that allows us to calculate the total number of flux lines n when given the total flux Φ and the

equation

$$\Phi = \Phi_0 n. \tag{2.2}$$

The flux can also be represented by the magnetic field B and area A of the superconductor:

$$\Phi = BA. \tag{2.3}$$

In the absence of magnetic field (including self-field), superconductors do not contain flux lines. The lowest magnetic field that results in flux lines is called the lower critical magnetic field B_{c1}. Because the magnetic field and the quantity of flux lines are linearly related, and each flux line contains a normal conducting core, there exists a magnetic field at which the material is no longer superconducting because it is overcrowded with vortex cores. This is called the upper critical magnetic field B_{c2}. Flux pinning occurs when the Lorentz force prevents flux lines from moving within the lattice. This phenomenon allows for loss-free current transport, allowing type II superconductors to form ideal electromagnets.

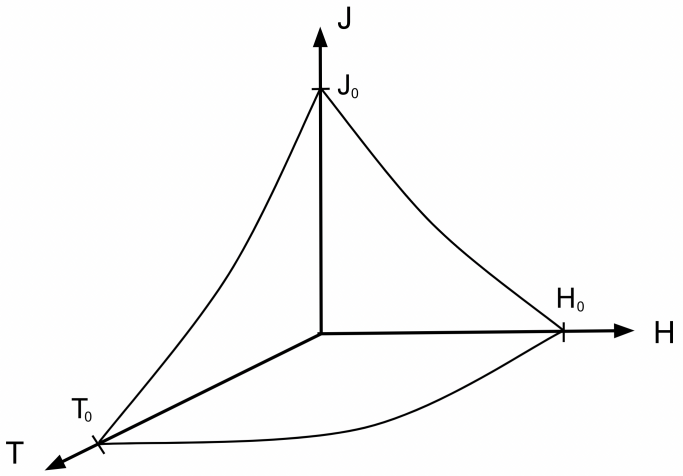

Figure 2-4: A visualization of the surface under which superconductors are in the loss-free regime. Adapted from [4].

The critical surface of a superconductor is often visualized on a three axis graph

(critical current density J_c, upper critical magnetic field B_{c2}, and critical temperature T_c). Each superconductor has different dependencies for the critical current density, magnetic field and temperature that must be experimentally determined. Points on or beneath this "surface" are in the loss-free regime, while those that appear above it are in the resistive regime [25]. In agreement with Figure 2-4, the critical current increases as the temperature decreases. By definition, all superconductors experience a resistance when exposed to currents above the critical current [35]. We exploit this resistance to control heating within the REBCO microstructure. The HTS tape's layers are discussed in detail in Section 2.4.

2.2.1 Resistive regime of REBCO superconductors

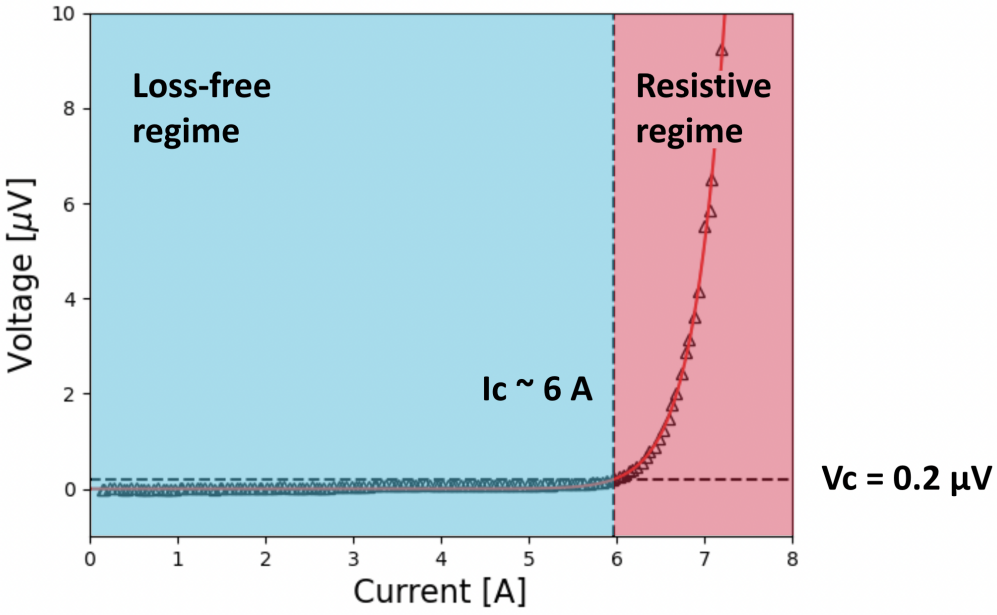

Figure 2-5: A current-voltage curve of a 2 mm length by 0.1 mm width bridged HTS tape at 77 K. The loss-free regime is marked in blue and the resistive regime is marked in red. The HTS tape's critical current is determined by the current at which the tape reaches the critical voltage, 0.2 μV. The REBCO bridge length (in this case, .1 mm) determines the critical voltage value [5]. This graph was modified from [6] with information from [5].

While producing the magnetic field for plasma confinement relies on REBCO's loss-free regime, this thesis takes advantage of the resistive regime. For the sake of

consistent measurement, this experiment considers an HTS tape to be in the resistive regime when it is experiencing any current above its critical current. The resistive regime is dissipative if flux lines move. Resistive heating, also known as joule or ohmic heating, occurs when electrons in a circuit collide with other electrons or ions, creating vibrations in the lattice of atoms. This kinetic energy is expelled as heat. The formula for power is

$$P = IV. \tag{2.4}$$

The power P (in W) dissipated in the tape is the product of the current I (in A) and voltage V (in V). This relationship may also be expressed using the resistance R (in Ω) as

$$P = I^2R. \tag{2.5}$$

When a current flows through a material, it always opts for the path of least resistance. Each metal or alloy has a different resistance, which can be calculated with the equation

$$R = \frac{\rho L}{A}, \tag{2.6}$$

where ρ is the elastic resistivity in Ωm, L is the length in m and A is the cross sectional area in m^2. This thesis uses the power imputed during each pulse, along with the material-based constants of an HTS tape, as a metric of measuring the REBCO's temperature during annealing [36, 37].

2.3 Thermodynamic calculations

The internal temperature of the REBCO can be calculated with knowledge of the pulse parameters. In the resistive regime, the power that travels through a component is equivalent to the heat transfer rate, $\dot{Q}$ (in $\frac{\text{J}}{\text{s}}$ or W). This process can be further

simplified by considering time t (in s) to discern the total heat transfer Q (in J):

$$Q = \dot{Q}t. \tag{2.7}$$

In the conduction equation for total heat transfer,

$$Q = mc_p(T - T_0), \tag{2.8}$$

m is the mass (in kg), c_p is the specific heat capacity (in $\frac{\text{J}}{\text{kgK}}$), T_0 is the starting ambient temperature of the tape, and T is the final temperature of the REBCO and the HTS tape in an isothermal system after a current pulse. Both T and T_0 are in K and the difference between them is represented by ΔT [37]. By rearranging Equation 2.8, we can define heat transfer as

$$\Delta T = \frac{Q}{mc_p}. \tag{2.9}$$

.

The specific heat capacity and electrical resistance can be found in the literature with known values from each of the HTS tape's components and assumptions regarding the thermal regime accessed by the heating pulse [36]. (Understanding that the majority of heating takes place above cryogenic temperatures allows us to avoid highly temperature dependent values.) With these equations and a known power input, we can provide an estimate of the peak temperature reached in the REBCO microstructure. Furthermore, this thesis utilizes a COMSOL Multiphysics simulation to better understand the effects of a heating pulse over an HTS tape. The software's package includes extrapolated values for the thermal diffusivity α, thermal conductivity k and specific heat capacity of each component of the HTS tape.

2.4 HTS tape structure

In order to allow high current transport, HTS tapes require many functional layers layers below the superconducting REBCO. The REBCO ($< 2\,\mu$m) lies on a buffer (approximately 200 nm), which provides a stencil for the ideal superconductor lattice [38, 39]. This is essential because the Hastelloy, which is mostly nickel, is incompatible with the REBCO, so the buffer layer acts as a structural and chemical intermediary. The REBCO crystal growth on top of the buffer layer is mostly (but not necessarily perfectly) uniform throughout each sample. The buffer and REBCO are stacked on a Hastelloy substrate ($38 \pm 3\,\mu$m) and surrounded by silver on both sides ($2 \pm 0.5\,\mu$m on the HTS side and $1 \pm 0.5\,\mu$m on the substrate side), all of which stabilize the sample [38]. Oftentimes, copper coats the silver layers, but we use copper-less tape because protons have a shorter attenuation length (on the order of micrometers) than neutrons (on the order of centimeters) [40]. In other words, protons would not penetrate past the copper, while neutrons do. This experiment uses Yttrium Barium Copper Oxide (YBCO) SuperOx tapes [41].

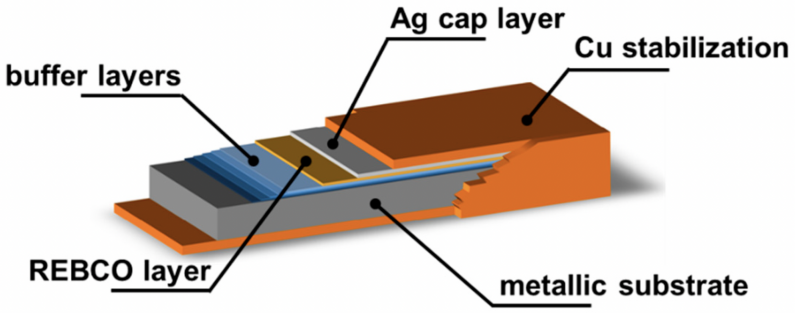

Figure 2-6: A schematic of the HTS tape's cross section [7]. The tapes used in this thesis do not have a copper stabilization layer, and the silver cap layer surrounds the entire tape.

2.4.1 Electrical resistivity

The electrical resistivity of metals vary with temperature. In order to figure out which metal within an HTS tape carries the current pulse, we must first discern which metal has the lowest resistivity. Table 2.1 shows each layer of an HTS tape's electrical

resistivity at both REBCO's critical temperature, 92 T, and at room temperature, 293 K. We neglect the buffer layer because it is only 200 nm.

Table 2.1: HTS tape components' electrical resistivity at the upper and lower temperature bounds [14, 15, 16].

Material	92 K	293 K
Silver	$3.8 \times 10^{-9}\,\Omega$m	$1.6 \times 10^{-8}\,\Omega$m
REBCO	$2.0 \times 10^{-8}\,\Omega$m	$1.4 \times 10^{-7}\,\Omega$m
Hastelloy	$1.1 \times 10^{-6}\,\Omega$m	$1.1 \times 10^{-6}\,\Omega$m

Table 2.2: HTS tape layer's dimensions used in calculations.

Material	Length [mm]	Width [mm]	Depth [μm]
Silver top layer	2	0.1	2
REBCO	2	0.1	< 2
Hastelloy	2	4	38
Silver bottom layer	2	4	1

Table 2.3: HTS tape layer's resistance at the upper and lower temperature bounds.

Material	92 K	293 K
Silver top layer	0.038 Ω	0.16 Ω
REBCO	0.040 Ω	2.8 Ω
Hastelloy	0.014 Ω	0.014 Ω
Silver bottom layer	0.0019 Ω	0.0080 Ω

This experiment uses HTS tapes with a bridge located at the center that decreases the sample's critical current. This is where the majority of resistive heating will take place, ergo the length, cross sectional area and mass of each layer is determined by either the 2 mm length by .1 μm width bridge shape or the unbridged portion of the same area (2 mm length by 4 mm width). Table 2.1 shows the electrical resistivity of each material, and Table 2.3 uses those values to find the resistance of each layer. The silver bottom layer has the lowest resistivity, and therefore this is where the bulk of the pulse current will travel while the REBCO is in the resistive regime. If we treat

the electrical resistivity value for silver as linear and analytically consistent with the literature, we get the equation [42]

$$\rho_{Ag,bottom}[\Omega\mathrm{m}] \;=\; 6.1\times10^{-11}\left[\frac{\Omega\mathrm{m}}{\mathrm{K}}\right] * T[\mathrm{K}] - 1.8\times10^{-9}[\Omega\mathrm{m}]. \tag{2.10}$$

This translates to a resistance of

$$R_{Ag,bottom}[\Omega] \;=\; 3.0\times10^{-5}\left[\frac{\Omega}{\mathrm{K}}\right] * T[\mathrm{K}] - 8.9\times10^{-4}[\Omega]. \tag{2.11}$$

Both of these equations are acceptable as long as we do not use negative values for the resistance or electrical resistivity (which occurs, according to this fit, below 30 K). Other values, such as the specific heat capacity and density D, are stable enough from 92 to 293 K to justify using a constant value [43, 19]. The volume V of the bridge acts as a singular thermal mass because each layer of the HTS tape is sputtered directly onto the previous, creating boundaries with high thermal conductivity [41]. Still, the individual specific heat capacities of each material is required to eventually find the heat transfer in the tape.

Table 2.4: HTS tape components' heat capacity and density values standardized at 293 K [17, 18, 19, 20, 21, 22, 23].

Material	$c_p[\frac{\mathrm{J}}{\mathrm{kgK}}]$	$D[\frac{\mathrm{kg}}{\mathrm{m}^3}]$
Silver	233	10490
REBCO	300	6400
Hastelloy	486	8200

Table 2.5: HTS tape layer's volume and thermal mass standardized at 293 K.

Material	$V[\mathrm{m}^3]$	$m[\mathrm{kg}]$
Silver top layer	4×10^{-13}	1.3×10^{-9}
REBCO	2×10^{-13}	4.9×10^{-6}
Hastelloy	3.0×10^{-10}	2.5×10^{-6}
Silver bottom layer	8.0×10^{-12}	8.4×10^{-8}

2.4.2 Radiation damage

Fusion reactors inevitably launch high energy fusion neutrons into the HTS tape, including the REBCO layer, strongly reduces its functionality [44]. When a fast neutron enters the superconducting lattice, it may hit and move an existing atom. This creates at least two defects: an interstitial where the displaced lattice atom lands and a vacancy where the atom used to be [45]. This duo, called a Frenkel pair, disrupts the order of the lattice. The REBCO loses critical current density (the local value of the critical current in the sample) in these specific sites; the large defects pin flux lines and the small defects scatter Cooper pairs [40]. On a macroscopic level, this decreases the critical current of the HTS tape [26].

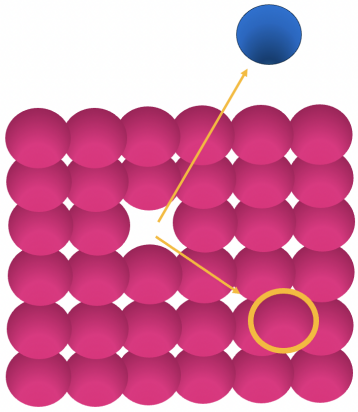

Figure 2-7: The incoming atom (blue) created a Frenkel pair by displacing the atom (pink, outlined in orange) previously in the lattice.

Neutrons are expensive and difficult to obtain at high energies and fluxes outside of a fusion reactor. Due to this obstacle, it is commonplace to emulate neutron damage with other forms of radiation [46]. The 14.1 MeV neutrons produced by SPARC lose energy each time they interact with matter, creating defects all-the-while. The attenuation length is the distance an uncharged particle will penetrate into a material before stopping. The primary factor that informs attenuation length is the size of the particle. For charged particles, the stopping power determines the penetration depth of the particle. More charge decreases the distance the particle can travel because it increases interactions with the surrounding (charged) matter, but has no bearing on the quantity of damage created at each interaction. Once stopped, the size of the

incoming particle determines the displacement that occurs in the lattice.

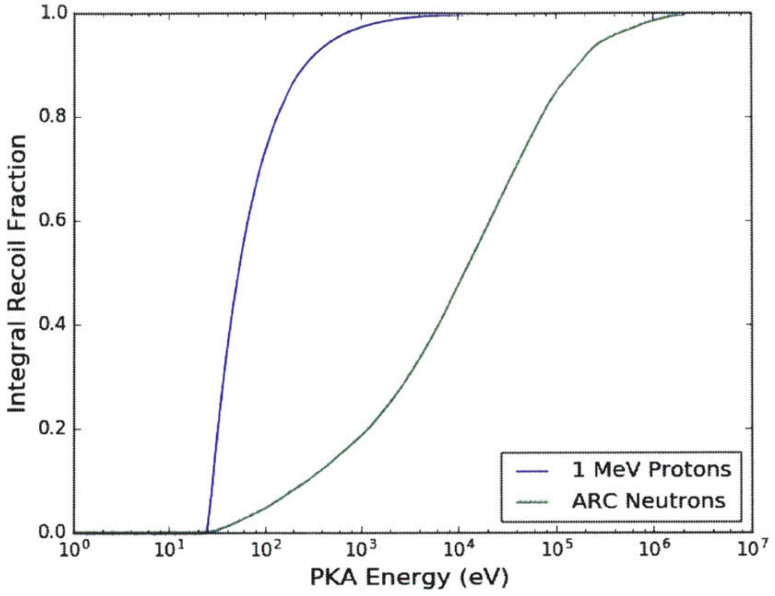

Figure 2-8: The PKA energy spectra of 1 MeV protons and ARC neutrons are very similar. The protons have a much steeper slope at low energies because they experience Coulomb scattering (as protons are charged particles) [8]. Still, this thesis treats the cumulative sum of damage created by the two particles as interchangeable.

Neutrons travel much further through matter than protons because they are uncharged and therefore are not drawn to or from charges in the matter. However, once the neutrons stop in a material, the damage created is very similar to that of a proton [45, 47]. This is because, at each interaction, the first atom displaced in the material lattice, the primary knock-on atom (PKA), is the only atom that touches the incoming radiation. The PKA then ricochets into other atoms in the lattice, carrying out even more damage in the surrounding area. Whether the PKA is pushed into motion by a proton or a neutron, the sustained damage is self-ion damage [48]. The amount of recoiling atoms in the lattice at lower PKA energies (beneath 10^4 eV and above the threshold energy) differs from 1 MeV protons to ARC neutrons, as seen in Figure 2-8. This is the largest difference between the two forms of radiation damage [8].

This experiment uses 1.2 MeV protons as a proxy for the neutrons found inside a tokamak. The value 1.2 MeV was chosen because, according to the attenuation length of protons and proven by the Stopping and Range of Ions in Matter Software

(SRIM) calculations in Brandon Sorbom's PhD thesis, protons at this energy create fairly uniform damage throughout the REBCO layer [8]. In self-field, critical current scales negatively and roughly linearly with 1.2 MeV proton fluence [12].

2.4.3 HECTOR

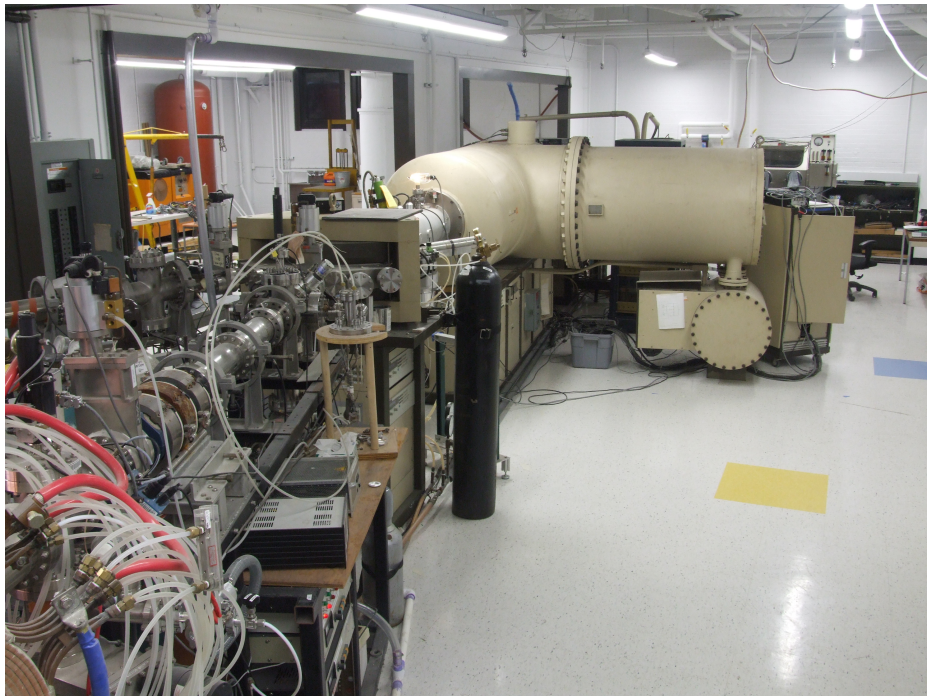

Figure 2-9: An image of HECTOR and the attached beam lines [9].

Cheaper and smaller than any device capable of producing high energy neutrons, particle accelerators are a practical solution [8]. This experiment uses the High Energy Cambridge Tandem for Observational Research (HECTOR) located in the Cambridge Lab for Accelerator based Surface Science (CLASS) Laboratory to produce 1.2 MeV protons. HECTOR is a General Ionex 1.7 MV tandem ion accelerator, also known as a Tandetron. Perhaps the most valuable perks of using a particle accelerator in lieu of a reactor include the ability to irradiate samples cyrogenically, without activating the samples, and at higher fluxes (in other words, at higher damage rates) [9].

While high energy protons (greater than 10 MeV) have the ability to activate materials, reactor-produced neutrons cause much more radioactivity. Figure 2-10

displays the dose rate of various activated materials after bombardment by high flux reactor neutrons, fast reactor neutrons, 12 MeV protons, and 12 MeV protons at a lower volume [10]. In each case, the protons caused significantly less radioactivity and dropped below the Nuclear Regulatory Commission's yearly limit of 0.1 $\frac{\text{rem}}{\text{h}}$ at 30 cm from the radiation source first [49]. Further, the 1.2 MeV protons selected for this experiment are an order of magnitude less energetic than the protons discussed in Figure 2-10 and do not activate the material.

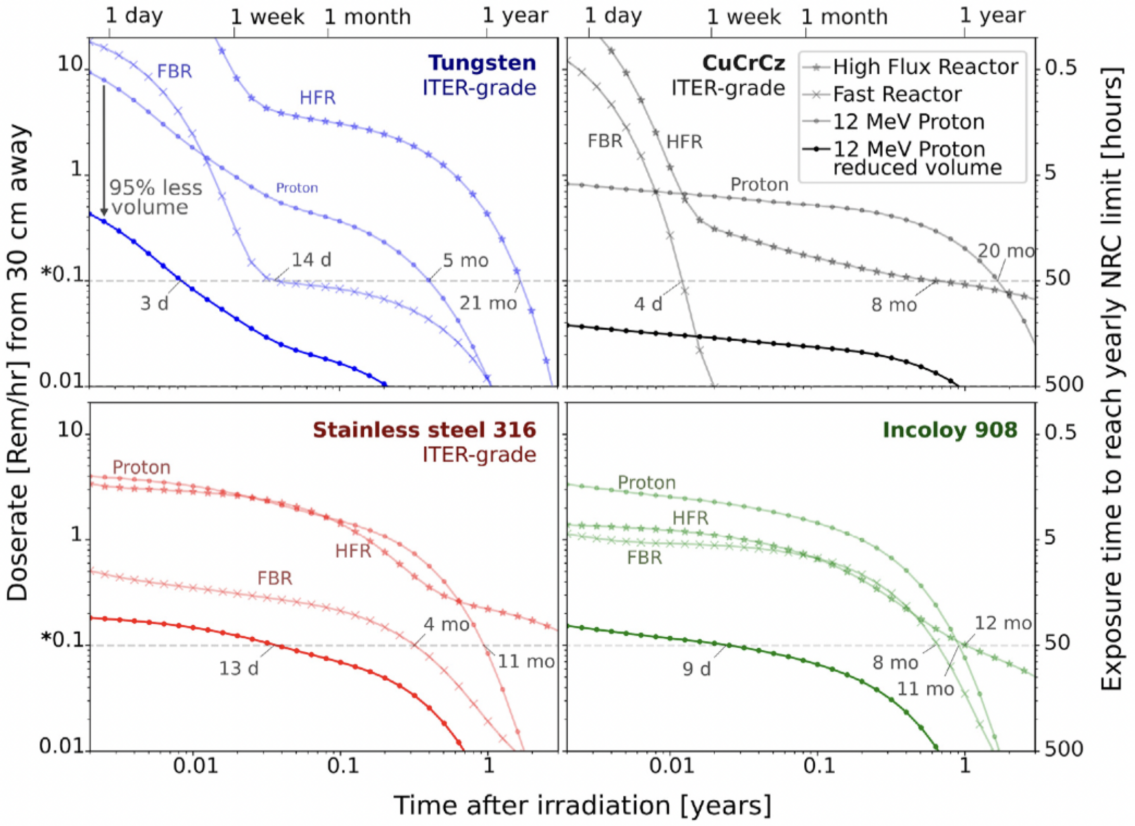

Figure 2-10: A FISPACT simulation of the radioactive hazard levels of protons and neutrons in tungsten, stainless steel 316, Incoloy 908 and copper chromium zirconium [10]. It is clear that protons offer the least activation.

Inside of the particle accelerator, at HECTOR's high energy end, nitrogen gas strips electrons. These electrons are selected by magnets and sent to the low energy end. At the low energy end, the electrons interact with an ion source to create the desired particle for irradiation. While HECTOR has two possible sources, this experiment only uses the National Electrostatic Corporation Source of Negative Ions

by Cesium Sputter (SNICS). The alternate source is primarily for helium and is irrelevant to this experiment [9].

SNICS works in conjunction with a solid cathode tip made of copper and filled with powder, which can be changed depending on the ion of choice (in this case, it is hydrogen) [50]. The beam is created when the cesium sputtering source forms negative ions from the ion-specific powder in the copper cathode, which then undergo an electron charge exchange with neutral cesium [11, 51]. The beam then passes through a focusing lens, or quadrupole, and is placed on the sample with x/y steerers, which control the position. The low energy magnet funnels the beam into the accelerator and the high energy magnet controls the experiment the beam interacts with (there are multiple set up on HECTOR) [9, 50, 11]. A Faraday cup lies after the low energy steering magnet, which blocks the beam from reaching the sample and reports the current when in place (and allows the beam to reach the sample when turned off) [50].

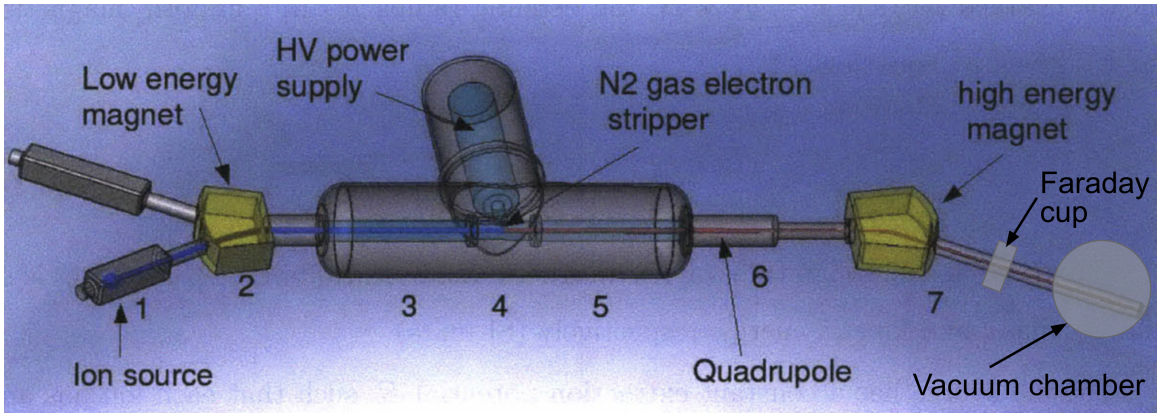

Figure 2-11: A Tandetron schematic [11]. Symbols represent the vacuum chamber specific to this experiment and Faraday cup.

2.4.4 Annealing and recovery

On an atomic level, annealing is the re-ordering of displaced particles in the microstructure. The thermal energy exerted on the lattice from a heat treatment (controlled resistive heating, in this case) increases the rate of diffusion of the atoms. This is because the temperature spike provides the energy needed to break bonds holding

interstitials in incorrect places. The energetically favorable locations for the interstitials to fall are the vacancies already in the lattice; if the damage is permanent, these defects will not resolve themselves [52].

When allowed to continue through the entire annealing process, materials can exhibit three stages: recovery, recrystallization, and grain growth. Recovery is the initial removal of defects as described above. Recrystallization is where new, defect-free grains replace the damaged ones. Grain growth is the coarsening of these fresh grains. Both recrystallization and grain growth decrease the mechanical strength of the material [53]. This experiment accounts for only the recovery stage. The movement of atoms during annealing in ceramics, such as REBCO, is much slower than that of metals because the atomic bonds are stronger [54].

Chapter 3

Experimental Setup

The HTS tape's critical current must be decreased with a laser skiver to make current measurements feasible with a 100 A current source. This is done by destroying controlled amounts of REBCO in a process called bridging. The bridged sample is placed in a sample holder, which attaches to a cryohead within the vacuum chamber. The cryohead maintains the temperature of the experiment, while the vacuum chamber (and the pumps attached to it) allow the experiment to exist in a vacuum. The proton beam is shaped into a circle and steered onto the sample during the irradiation portion of the experiment. During the annealing portion, a box capable of delivering variable current pulses as large as 2000 A and as fast as 100 ns connects to both ends of the sample via the vacuum chamber's high-current feedthrough.

3.1 Laser bridging

Figure 3-1: A drawing of a bridged HTS tape. The dark gray areas have been etched by the laser, creating a bridge of pristine REBCO.

In order to make our experiments more manageable, we to decrease the amount

of superconducting REBCO in an HTS tape. During bridging, we purposefully reduce the cross section of the superconductor by etching through the layers in specific geometric designs with a laser. This experiment uses a template with rectangles on the top and bottom of the tape that leave a thin (2 mm length by 0.1 mm width) "bridge" in the center of the sample. The smallest portion of functioning superconductor decides the entire sample's critical current. Therefore, an unirradiated and bridged sample's critical current is dictated by the size of the bridge. The relationship between the bridge size and the tape's critical current can be represented by the equation

$$I_{\text{c,unbridged}} = \frac{x_{\text{unbridged}}\, I_{\text{c,bridged}}}{\eta\, x_{\text{bridged}}}. \tag{3.1}$$

$x_{\text{unbridged}}$ is the width of the entire sample, x_{bridged} is the width of the bridge only, $I_{\text{c,unbridged}}$ is the calculated critical current of the HTS tape, $I_{\text{c,bridged}}$ is the measured critical current of the bridged sample, and η is the bridging efficiency (the largest possible value being 1). The bridging efficiency is a scaling factor that represents the effectiveness of the laser process, defined as what we observe versus predict for a given geometry and set of skiving parameters [55].

All of the tapes used in this thesis were bridged using the laser skiver at Commonwealth Fusion Systems (CFS). The device, a Bright Solutions Wedge XF 532 OEM Integrated Marker, is paired with Scanner Application Software's Scanner Application Modules Light (SAMLight). The beam propagation ratio refers to how closely to a perfect Gaussian the laser beam can be focused, with the perfect and physically unattainable value being 1 [56]. Most high quality lasers—including the Bright Solutions Wedge XF 532 OEM—have beam propagation ratios below 1.3 [57]. This allows us to assume high laser accuracy and a bridging efficiency of 1.

This experiment uses samples with 2 mm length by 0.1 mm width bridges. The unbridged tapes are 4 ± 0.1 mm wide, so the experimental critical currents measured are 40 times smaller than the theoretical critical current of the unbridged tape [38]. Unexpected variation in the critical current may occur because the REBCO crystal

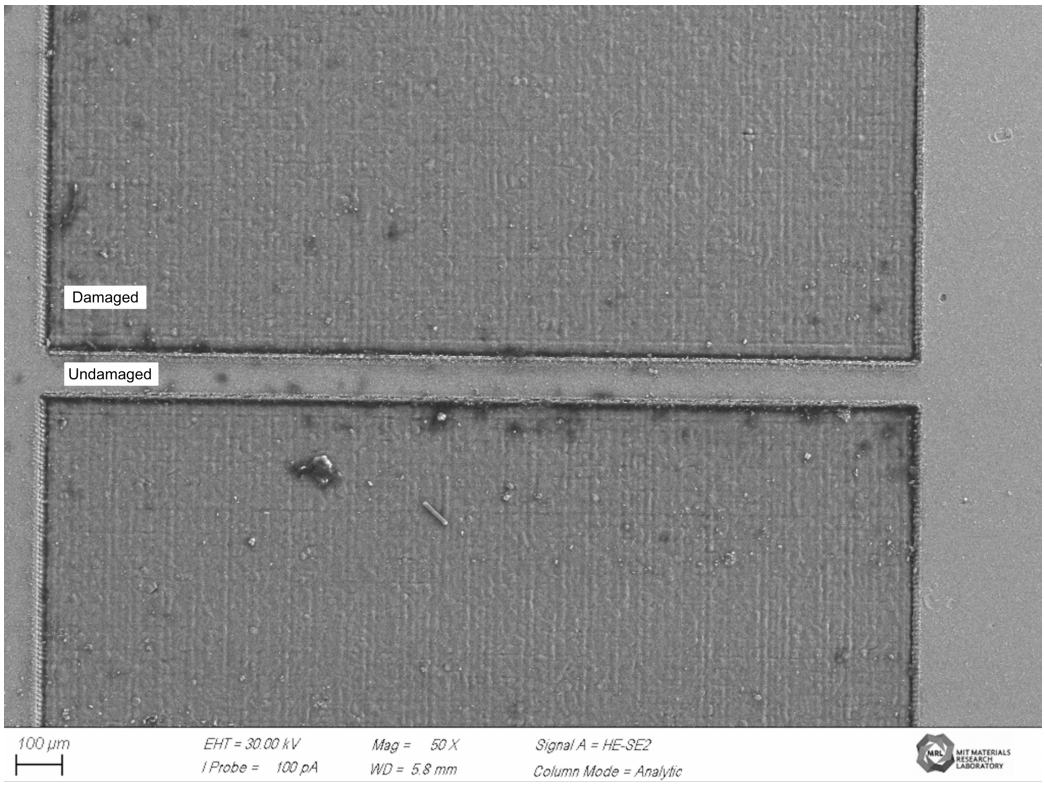

Figure 3-2: A scanning electron microscope image displaying the accuracy of a 2 mm length by 0.1 mm width bridge made with CFS's laser skiver.

growth is not necessarily perfectly uniform and defects in the microstruture unrelated to radiation damage are inevitable. If the portion of REBCO the bridge happens to capture exhibits defects unrelated to radiation, the critical current of the sample may be lower than anticipated [55].

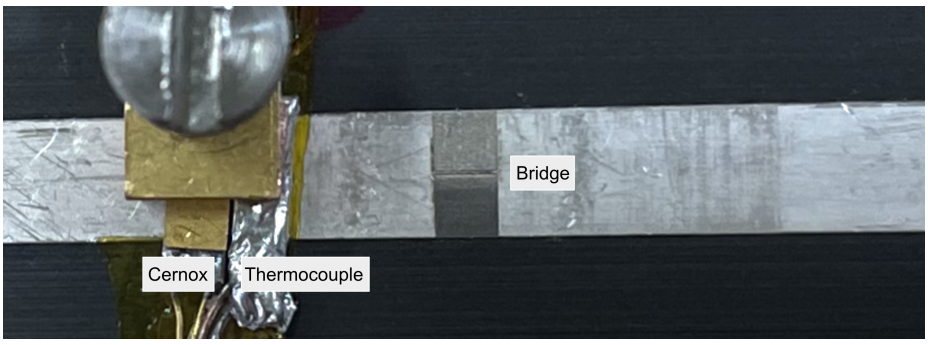

Figure 3-3: An image of a 2 mm length by 0.1 mm width bridged HTS sample mounted in version two of the sample holder. The Cernox temperature sensor and thermocouple are visible on the left of the image and discussed in Section 3.2.

3.2 Sample holder

The sample holder exists to thermally couple the HTS tape to the adapter (which is temperature regulated and attached to the cryohead), as well as electrically connect the sample to current pulses and transport current measurements. The sample holder is electrically insulated from the HTS tape with Kapton, an electrically insulating polymide that can be purchased as an adhesive cryogenic tape [58]. Two copper blocks bolted into the sample holder (and pressed onto the sample with indium) connect the current leads. Pogo-pin voltage taps touch the HTS tape on either side of the bridge [12]. This allows for four-terminal measurements, a highly accurate method for measuring resistance that relies on two separate current delivering and voltage sensing pairs [59]. The system is pressed flat by a copper sandwich top, or compression stage.

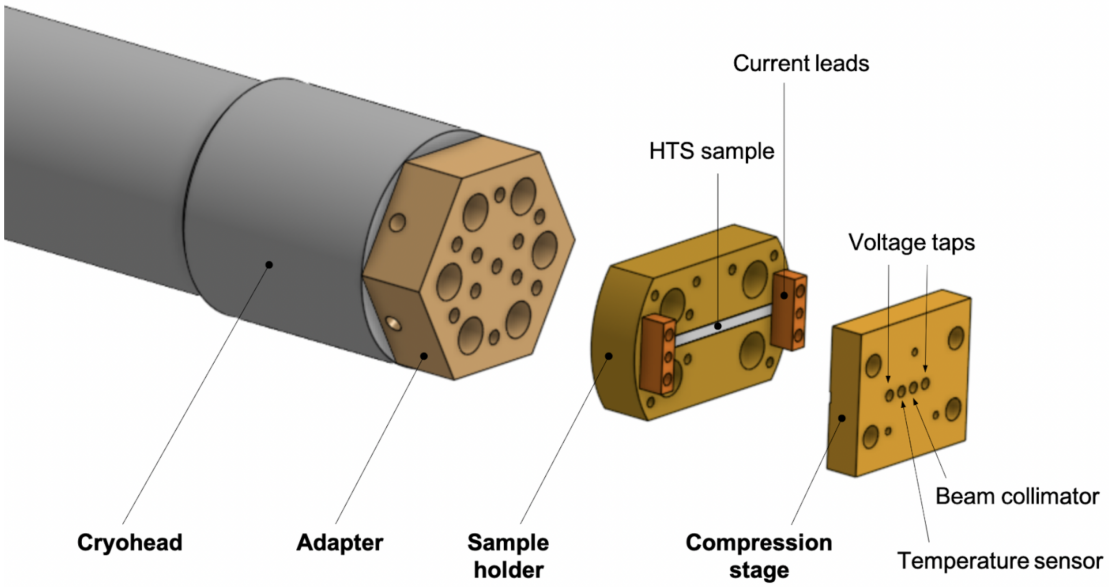

Figure 3-4: The target stage in an exploded computer aided design (CAD). The four major parts are the cryohead, the adapter, the sample holder and the compression stage [12] This image features version one of the sample holder and its corresponding compression stage.

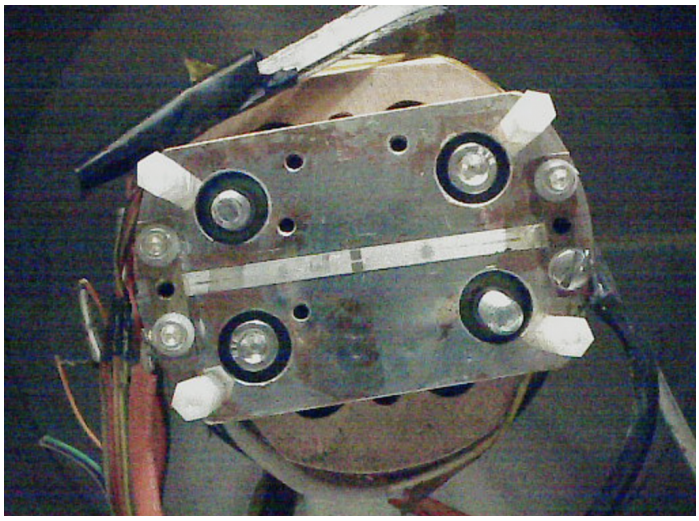

Figure 3-5: Version one of the sample holder *in situ*. This image was taken before the compression stage was added.

3.2.1 Version one

The duration of this thesis coincided with two generations of sample holders. The first was a 1.9 cm thick copper block. This sample holder can apply a positive 90 V bias to prevent secondary electrons from escaping. It worked in junction with a Cernox temperature sensor, which does not have a fast enough sampling rate to reliably capture the temperature change in an HTS tape from a millisecond current pulse [12]. Another fault of this version is that it requires samples to be at least 5 cm long. This has the potential to make collaborations with other research groups more difficult, as the lengths HTS tapes vary greatly from laboratory to laboratory (and are often too small for this sample holder). For example, the magnet bore in the 15 T magnet at Technische Universitat Wien, which we work with frequently, requires 3 cm samples [27]. Lastly, this sample holder is quite difficult to assemble and has a noticeable temperature gradient throughout the holder (roughly 10 K).

3.2.2 Version two

The sample holder presently installed in the experiment eliminates many of its predecessor's faults. It is compatible with both a Cernox temperature sensor and a thermocouple for temperature measurements (expanded on later), much easier to put

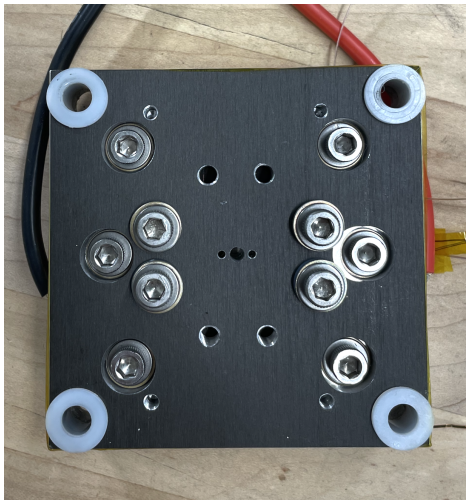

Figure 3-6: Version two of the sample holder with an installed HTS tape and the corresponding compression top before being installed inside the vacuum chamber.

together, and allows for 3 cm long samples. In addition to the positive 90 V bias on the sample holder, a secondary electron emission plate lies above the sample and is charged with a negative 90 V bias. The negative bias on the secondary electron plate repels electrons, working to prevent electrons from ricocheting off the HTS tape and leaving the system after proton irradiation. In parallel, the positive bias on the sample holder pulls escaping electrons back to the HTS tape. This suppression of secondary electrons allows us to obtain the true proton beam current on the sample. Version two of the sample holder still displays a small temperature gradient (approximately 3 K), which will hopefully be solved in the next iteration.

3.2.3 Thermocouple

The temperature on the surface of the HTS tape is measured with a Type E thermocouple. This thermocouple has a stronger signal and higher accuracy in cryogenics than other types. It has a range of 3 K to 1143 K and an accuracy of ± 1.7 K. Type E thermocouples are made of a positive leg (a 90% nickel and 10% chromium alloy called Chromel) and a negative leg (a 95% nickel, 2% aluminum, 2% manganese, and 1% silicon alloy called Constantan) [60]. These different metals touch at a spot-welded junction, which produces a thermo-voltage that can be translated into a temperature when heated or cooled to a temperature different than that of the cold junction (which functions as a control).

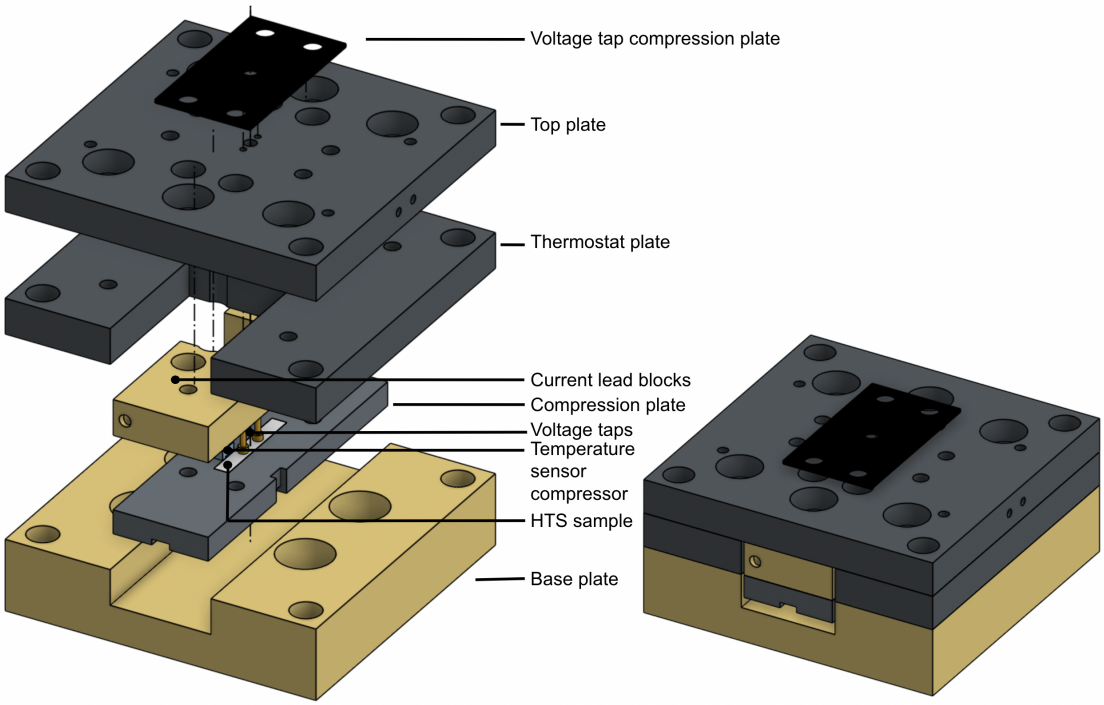

Figure 3-7: Exploded (left) and normal (right) views of version two of the sample holder's CAD. The thermocouple and Cernox temperature sensor are both pressed under the temperature sensor compressor.

The thermocouple in this experiment is pressed onto the sample (between the sample holder and the temperature sensor compressor). A layer of 25 μm Kapton prevents the thermocouple from electrically connecting to the sample, but is thin enough to allow to thermocouple to detect temperature change on the surface of the HTS tape. The Kapton must be accounted for, along with the layers of silver, Hastelloy, and buffer, when calculating the internal temperature of the REBCO. The thermocouple is calibrated against the temperature sensors pressed against the tape, within the sample holder and on the target head. The thermocouple has a gauge size of 38, which translates to about 0.1 mm in diameter. Having such a small thermocouple allows it to not disrupt the sample holder set up and, more importantly, not disrupt the thermal mass of the system.

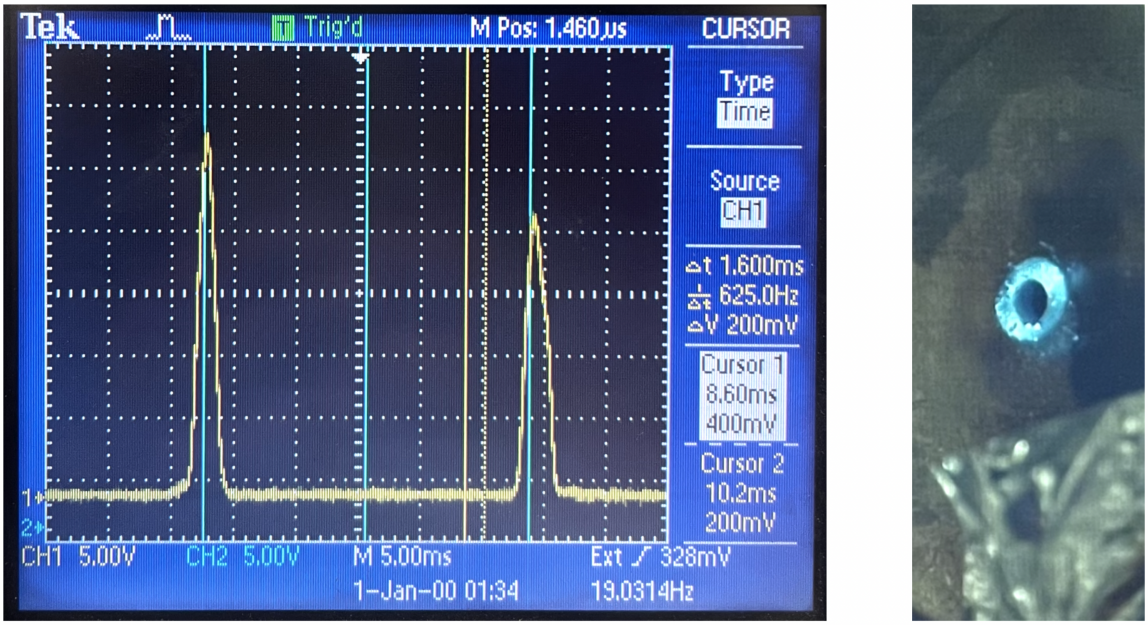

Figure 3-8: A photo of the oscilloscope measuring the BPM's signal (left) and the corresponding proton beam on the collimator (right). The two peaks represent the x and y locations.

3.3 Proton beam

Irradiation runs were conducted with HECTOR and utilized 1.2 MeV protons to damage the HTS tape until it retains less than 10% of its pristine critical current. Before making contact with the sample, the proton beam passes through the beam profile monitor (BPM). The BPM informs the shape and location of the proton beam by sweeping it (twice a revolution, one for the x-direction and one for the y-direction) with a rotating helical wire [61]. The wire produces secondary electrons when it makes contact with the beam, which are recorded by a cylindrical collector. The values the BPM measures are directly proportional to the beam current, so it can display the beam's x and y profiles in real time. The BPM allows us to calibrate the beam size as a Gaussian shape, guaranteeing that only the full-width half maximum passes through the collimator.

After interacting with the BPM, the proton beam goes on to hit the Faraday cup, a positively biased metal cup and micro-ammeter (this is how we determine the amplitude of the beam current). The Faraday cup blocks the sample from the

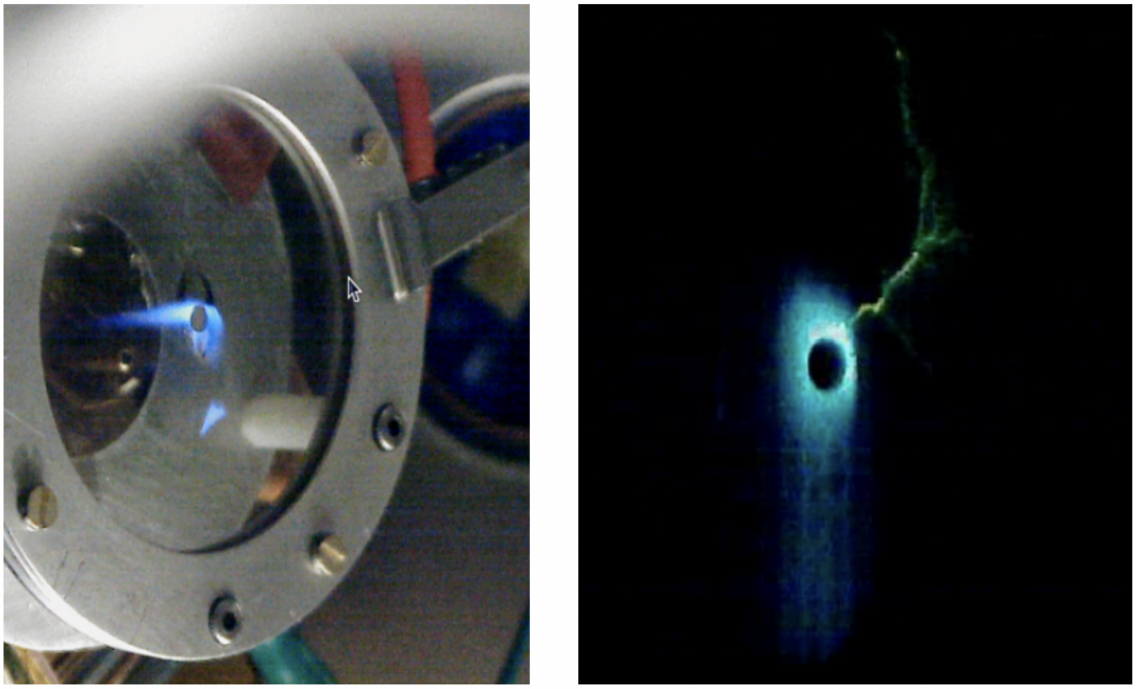

Figure 3-9: Both of these images depict 1.2 MeV proton beams from the now-decommissioned Deuterium Accelerator-based Neutron-producing Tandem Experiment (DANTE) on the collimator. A light shining into the chamber makes the setup visible (left) in one image, while an arc is observable in the other (right).

proton beam and serves as a safe surface to roughly align the beam on [11]. When the Faraday cup is lifted, the proton beam enters the vacuum chamber and passes through a 3 mm hole in the center of a gold-coated glass collimator. The protons hitting the collimator appear as a blue light, which makes beam focusing, or shaping, convenient. This blue light is a result of ion beam-induced luminescence, a phenomenon where an ion beam (protons) excites the atoms in a target, which expel energy as visible light [62]. This process is called scintillation. Beyond the collimator, the beam passes through a 4 mm hole in the electron suppression plate and, finally, to the sample via the 3 mm hole in the sample holder.

3.4 Vacuum chamber

The HTS sample sits in line with the proton beam and inside of a vacuum chamber. The chamber is pumped down to a vacuum with two roughing pumps (both

Edwards XDS5) and a fine pump (Pfeiffer Vacuum Turbopump 240) and kept beneath 20 K with a cryocooler (the AL230 from Cryomech). The cryocooler, however, is not temperature regulated. A temperature adaptor with four heaters and a Cernox temperature sensor adheres to the cryohead and controls the sample temperature via a proportional-integral-derivative (PID) loop [12]. We maintained a 20 K and 5×10^{-6} Torr environment during irradiation and pulsing.

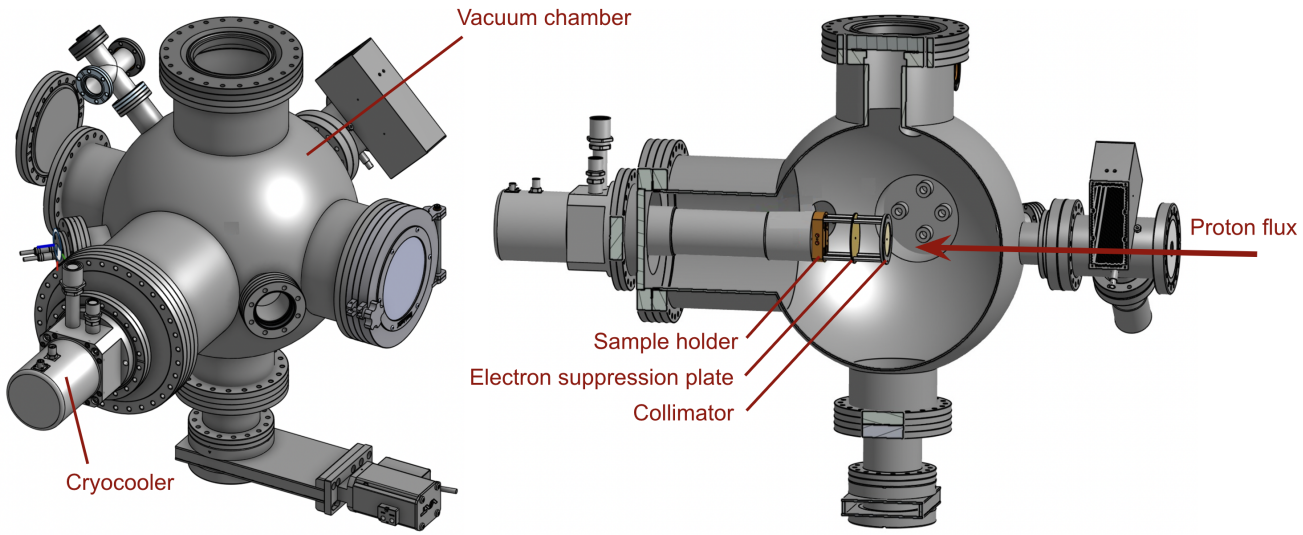

Figure 3-10: The external (left) and cross sectional (right) CAD views of the vacuum chamber. The cross section includes an installed sample in version one of the sample holder and labels where the proton beam enters.

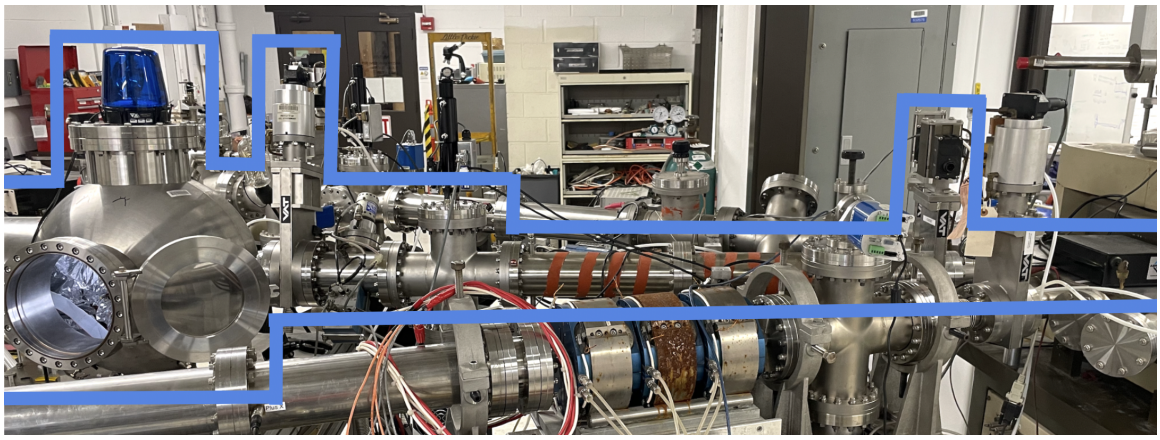

Figure 3-11: The vacuum chamber and attached beam line, outlined in blue.

3.5 Pulse box

The experimentation in this thesis relies on a box with fast, high current pulsing capabilities. The pulse box connects to the HTS sample inside the vacuum chamber through current leads accessible outside the chamber. It is capable of sending square waves as short as 100 ns and as large as 2000 A. (However, preliminary testing revealed that pulses at such a large amperage will burn the tape.)

The pulse box works by taking an input from a waveform generator (Rigol DG4062). This is what defines the pulse length parameters and, although the waveform generator has varied capabilities, this experiment exclusively uses 9.4 V square waves with a 4.7 V offset. This is because the gate driver (FOD3182), the first electrical component to interact with the waveform generator's voltage pulse, requires at least 8.5 V for reliable functionality. The offset is required because the gate driver is not compatible with negative voltages [63].

The gate driver is powered by a 15 V and 1 A constant external power supply. When it is triggered, it produces a pulse identical in duration at 15 V and 3 A. The gate driver contains an optocoupler that keeps the circuits separated and reduces any noise from a slow ramp up and down (into a square wave) that the pulse generator may produce. Although this is not an issue with the waveform generator, this system was originally designed using a 555 timer and is therefore compatible with less exact electrical components. The gate driver allows the pulse to meet the minimum amperage required to switch the insulated gate bipolar transistor (IGBT) (IXXK200N65B4-ND).

The IGBT keeps the circuit with the HTS tape and a 25 V, 1 F capacitor open. The capacitor is charged with a variable power supply (GwInstek GPD-3303D) prior to each current pulse, as the voltage determines the amplitude of the current pulse. For 400 A pulses, the capacitor must be charged to 5 V.

When the IGBT receives the pulse from the gate driver, it completes the circuit and allows the capacitor to discharge over the HTS sample. An oscilloscope (Tektronix TDS2004) measures the final pulse amplitude over a shunt resistor, the gate

drivers output, and uses the waveform generator as a trigger. (The gate driver often malfunctions when accidentally touched and is therefore not directly soldered onto the motherboard, but rather connects to a soldered integrated circuit socket.)

The box has a switch that connects and disconnects it from the HTS tape, as well as a switch with modes for charging the capacitor to the value selected on the power supply, discharging the capacitor over a resistor, and sending pulses through the tape.

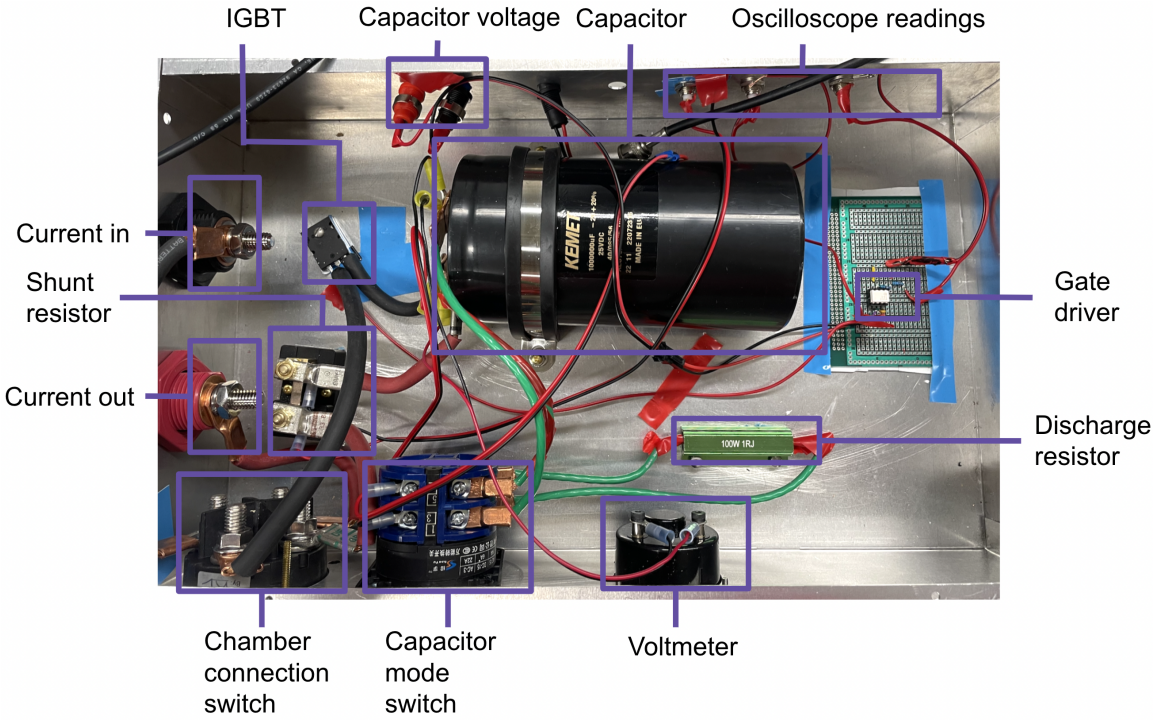

Figure 3-12: The inside of the pulse box.

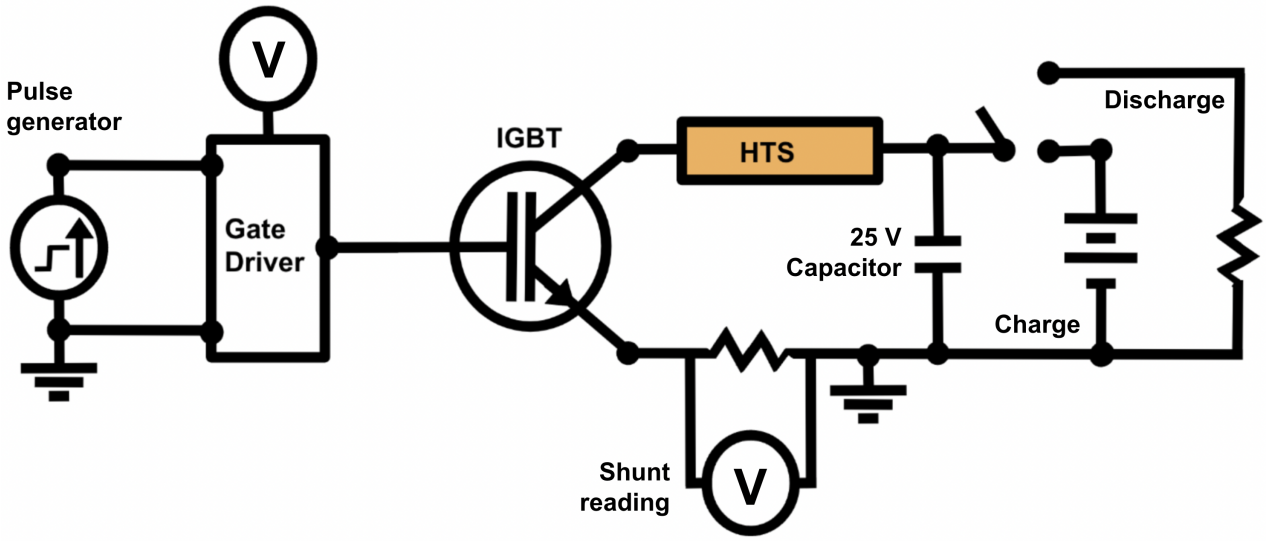

Figure 3-13: A simplified circuit diagram of the pulse box.

Chapter 4

Methodology

Figure 4-1: The graphical user interface (GUI) displaying the observed environment. The temperature is measured in the Cernox sensors in the target cryohead, sample holder, and on the sample, the pressure is measured in the vacuum chamber, and the heating power refers to the wattage of the heaters and coolers attached to the chamber. The temperature can be set from the GUI and the beam off button lifts the Faraday cup. The other GUI function utilized in this experiment is the critical current measurement.

4.1 Current measurements

Figure 4-2: The monitors, controllers and current sources that power critical current measurements and record the state of the vacuum chamber.

Throughout this experiment, we measure the HTS tape's critical current with *in situ* transport current measurements. This quantifies the amount of damage or recovery the HTS tape has undergone. Each measurement works by slowly increasing the amount of current run through the tape, all-the-while a nanovoltmeter records the voltage. The current ramping stops when the abort voltage is reached. $1\,\mu$V/cm is commonly accepted as the electric field criterion to define the critical current in an HTS tape. For a sample with a 2 mm long bridge, this means a value of $0.2\,\mu$V, which is an order of magnitude above the noise level in the system. The abort voltage in this experiment is $10\,\mu$V [12].

The data acquisition takes place over a graphical user interface (GUI) written in

Python. The recorded data points are fit using the *curve_fit* package from *scipy* to the power law. The critical current is calculated using

$$V = V_c \left(\frac{I}{I_c} \right)^n . \tag{4.1}$$

V is the voltage (in V), V_c is the critical voltage ($0.2\,\mu$V), I_c is the critical current (in A) and n is the n-value, a constant. The fit does not consider data points with a voltage above $50\,\mu$V because they are reliably in the resistive regime and create unnecessary noise when finding the curve fit.

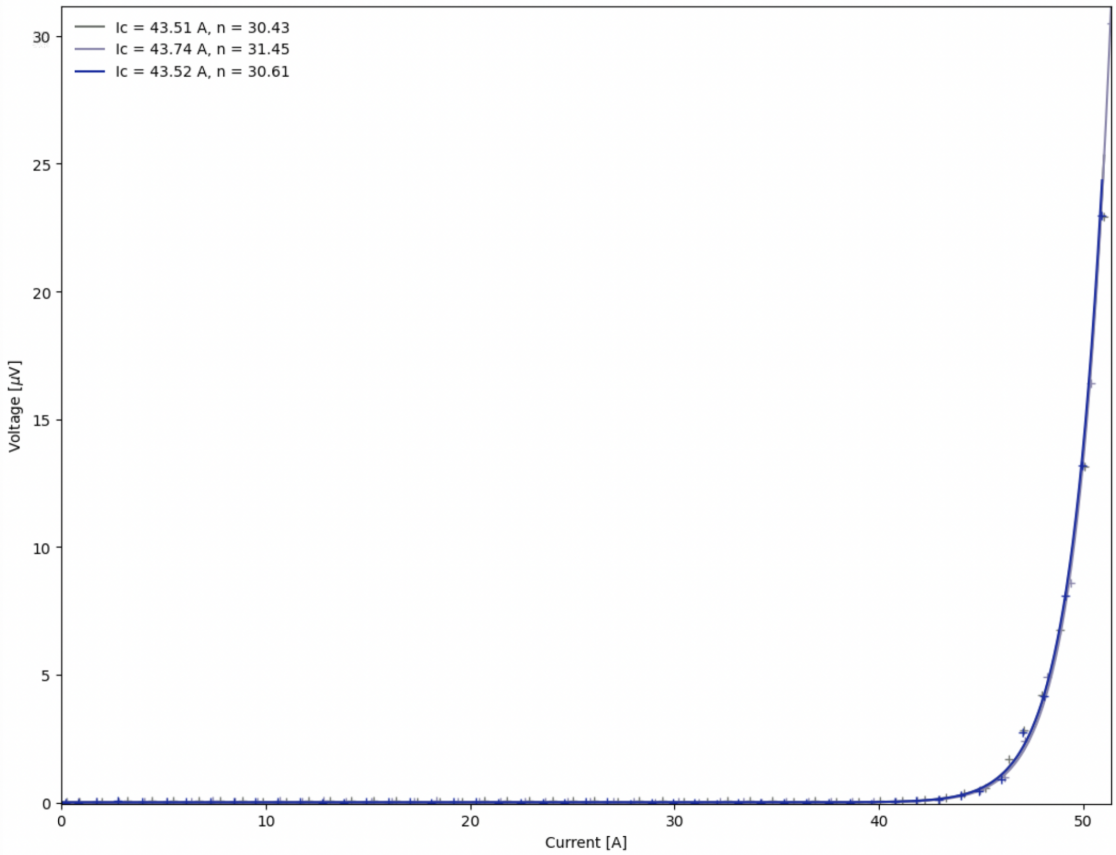

Figure 4-3: Three measurements of a pristine tape at 20 K.

4.2 Pulsing parameters

The fast pulses in this experiment reduce the risk of burning the sample. Square pulses specifically allow for binary analysis of heating exposure. Calculating the amount of time the REBCO layer is exposed to each current is much simpler when integration is not required (a benefit of a square wave over a sine wave pulse). Furthermore, because the amount of power exposed to the HTS tape remains mostly constant in a square wave pulse, we do not risk attributing any recovery to incorrect powers. It is important to note that the capacitor experiences a discharge that prevents the pulse from being a perfect square wave. However, we neglect this phenomenon because the capacitor's large capacitance (1 F) and constant recharging (between each pulse) keeps the square wave effectively pristine.

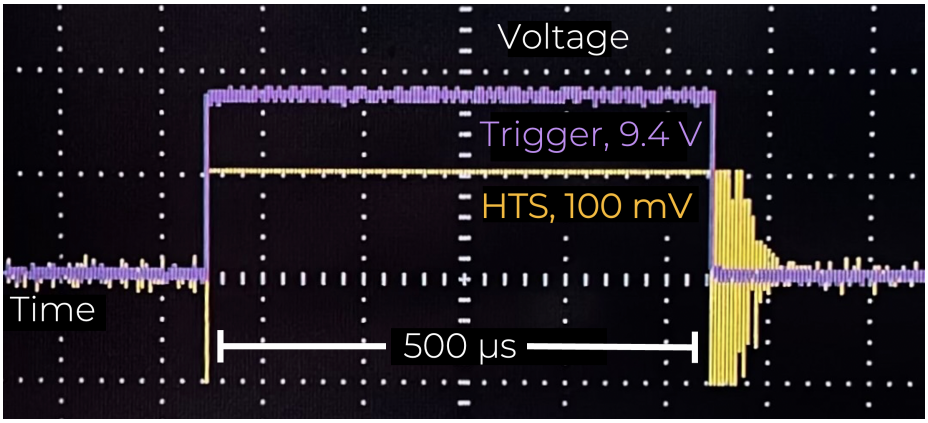

Figure 4-4: An oscilloscope reading of a 200 A pulse, along with the trigger signal from the waveform generator, over a tape with a 2 mm length by 0.4 mm width bridge [13].

4.2.1 Duration and amplitude

This thesis aims to iterate through various durations to find that with maximum recovery. Trials were held at 400 A. The current density can be found by dividing the total current by the cross sectional area through which it travels. Because we know that the 400 A conducts through the bottom silver layer while the REBCO is in the resistive regime, we can assume that the current density is $1 \times 10^{11} \frac{\text{A}}{\text{m}^2}$. This

value was chosen because it is well below the system's full capacity and only required charging the capacitor to 5 V. The first trial at 400 A successfully displayed annealing, and therefore more information at this amperage was perused throughout the of the experiment.

After each pulse (and respective critical current measurement), we increase the pulse duration. If there is no recovery, we doubled the duration of the following pulse. However, if there is recovery, we increase the time step linearly. By the nature of this experiment, every tape experiences an inevitable burn when it is given too much energy, as the length parameter is consistently increased until the tape burns.

4.3 Temperature measurement

The thermocouple is attached to a Keithy Digital Multimeter 6500, which records the temperature change only after the waveform generator's trigger and has a sampling rate of 1 fracMSs. Throughout this thesis, we attempted to obtain the temperature in two ways: by measuring the power discharged in and the external temperature of the HTS tape. Both of these methods require calculating the internal temperature of the REBCO micro-structure using the material properties found in the literature search at the beginning of this thesis in addition to the measured variable.

4.3.1 Temperature based on power applied

Assuming the entire 400 A current will travel through only the bottom silver layer, which exhibits the least resistance at the bridge (while the REBCO is in the resistive regime), and utilizing Equations 2.5 and 2.11, we can identify the power (in W) in the tape as

$$P[\mathrm{W}] \quad = \quad 4.8 \left[\frac{\mathrm{W}}{\mathrm{K}}\right] * T[\mathrm{K}] - 140[\mathrm{W}]. \tag{4.2}$$

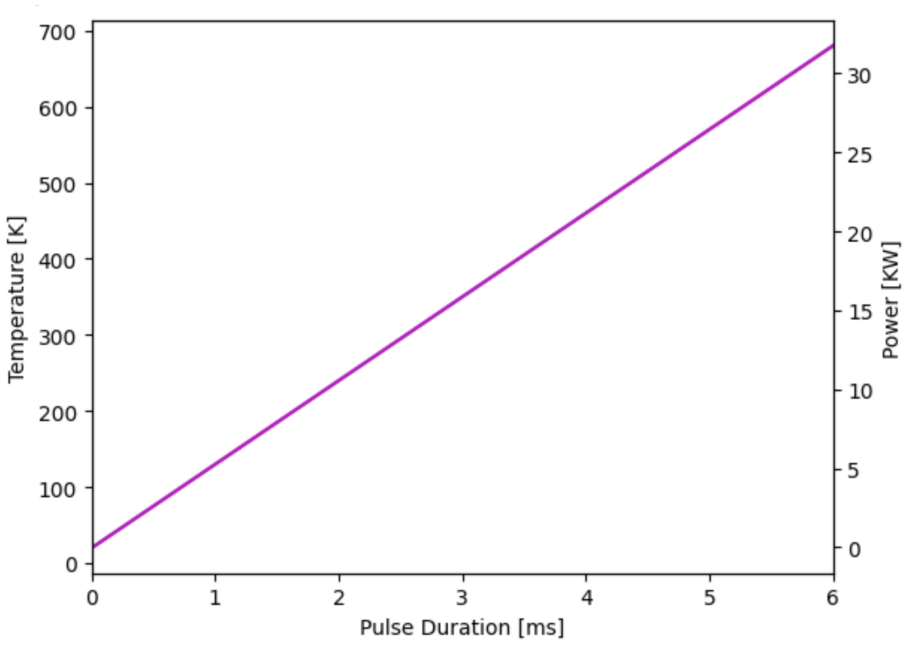

Figure 4-5: The temperature and power experienced in the tape as a function of 400 A pulse duration, as found with Equations 4.5 and 4.6.

Because we cannot have a negative power, we make the assumption that the power is 0 W before 30 K. Although this is not actually true, the power grows rapidly enough to justify this generalization. The mass of the bottom layer of silver is 4.16×10^{-8} kg and the specific heat capacity is 233 $\frac{\text{J}}{\text{kgK}}$ [17]. The ambient temperature of the experiment is 20 K. Combining Equations 2.9, 2.12, and 4.2 teaches us that

$$\Delta T = \frac{I^2 R \Delta t}{c_p m}. \tag{4.3}$$

Substituting in our known values from Section 2.4.1, and the non-temperature dependant resistivity value at the entrance of the resistive regime reveals:

$$\Delta T[\text{K}] = 1.1 \times 10^5 \left[\frac{\text{K}}{\text{s}}\right] * t[\text{s}]. \tag{4.4}$$

Solving this equation for the maximum temperature in the tape at a given time yields

$$T[\text{K}] = 1.1 \times 10^5 \left[\frac{\text{K}}{\text{s}}\right] * t[\text{s}] + 20[\text{K}]. \tag{4.5}$$

By the same logic, the pulse duration dependent equation is

$$P[\mathrm{W}] \quad = \quad 5.3 \times 10^5 \left[\frac{\mathrm{W}}{\mathrm{s}}\right] * t[\mathrm{s}] - 44[\mathrm{W}]. \tag{4.6}$$

4.3.2 Temperature based on external measurement

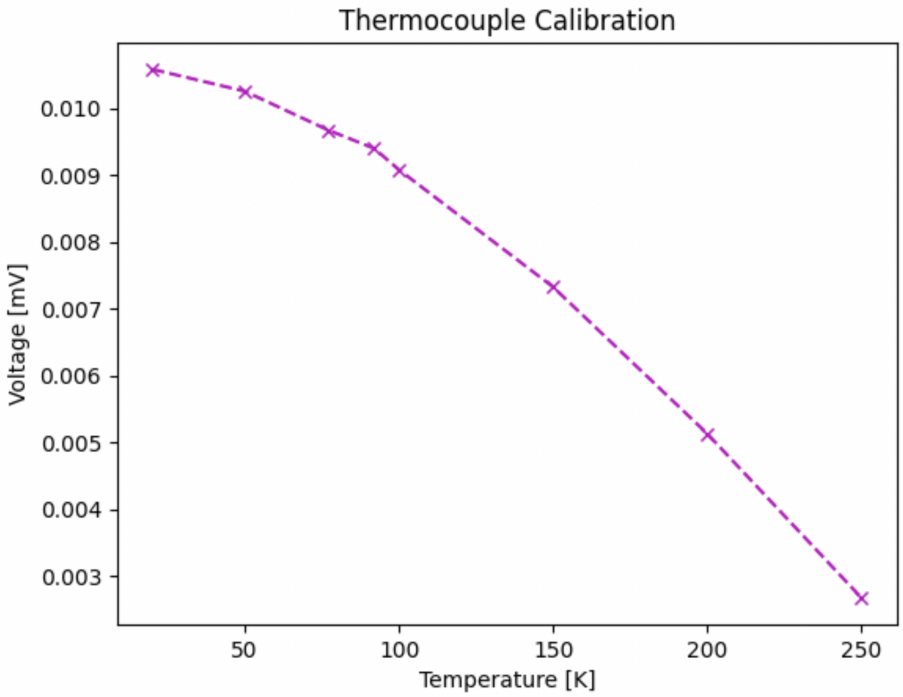

Figure 4-6: The thermocouple calibration below room temperature with a line plot.

The thermocouple, which was calibrated to the Cernox sensor in 50 K intervals, reads the temperature on the surface of the HTS tape in line with and 40 mm from the bridge. However, a COMSOL Multiphysics simulation of the heat transfer in an HTS tape during a current pulse revealed that this distance is too far to measure an increase in the REBCO microstructure's temperature at the bridge while treating the entire sample holder as a cold reservoir at 20 K [64].

The simulation in Figures 4-7 and 4-8 applied a 1 ms pulse of 2.56×10^5 W (an overestimation of the power that this layer of silver experiences at 400 A found by with the room temperature resistance of silver) directly to the silver on the bridge of the sample. Assuming that the REBCO is heated by the silver efficiently enough to share

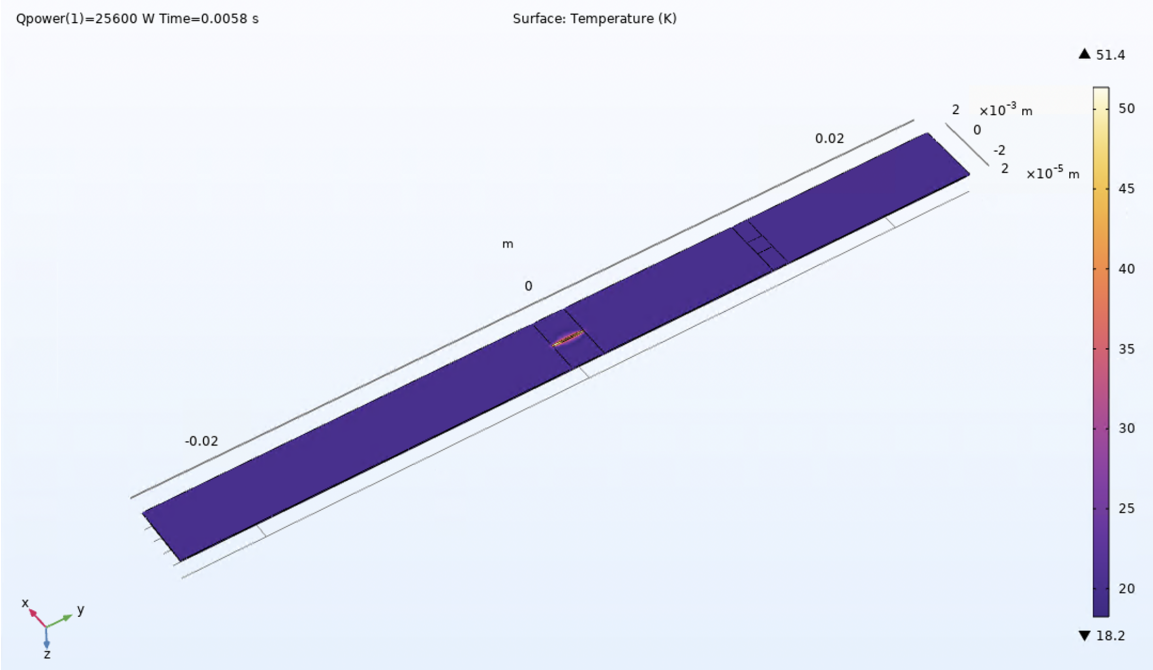

Figure 4-7: A model of a bridged HTS tape experiencing a 2.56×10^5 W and 1 ms pulse over the top silver layer. This image is from the peak of the pulse. Note now the majority of the tape displays no temperature change.

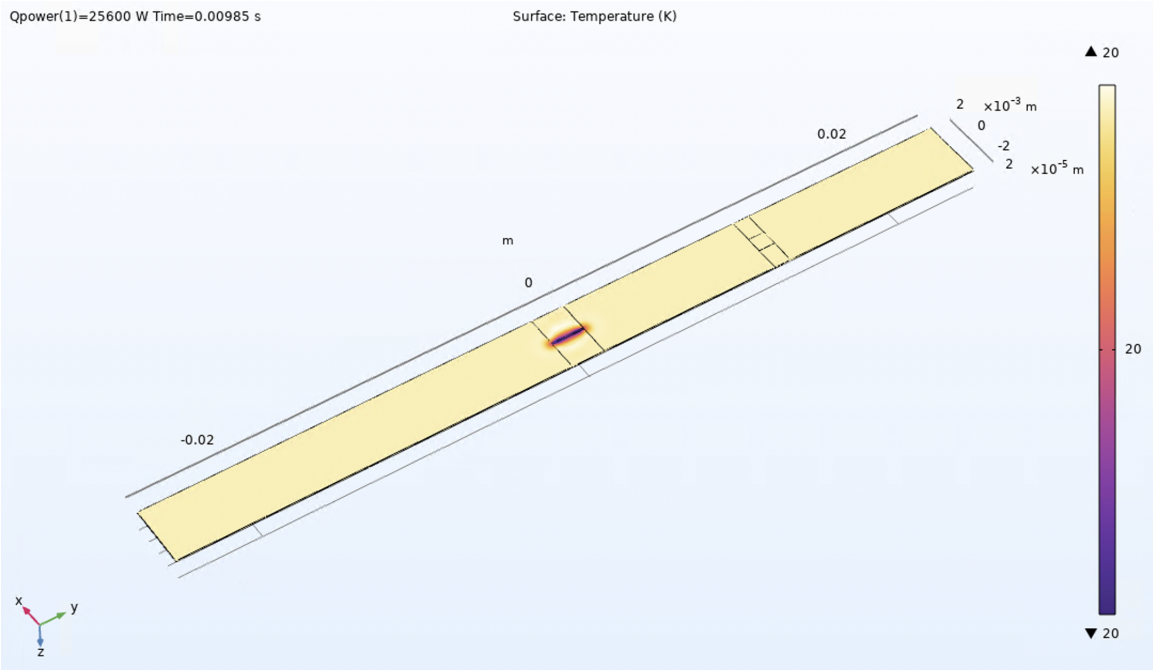

Figure 4-8: The same HTS tape just after the pulse concluded. Note the continued lack of temperature change.

a maximum temperature, we can give the REBCO a maximum value of 51.4 K for this pulse. However, increasing the pulse duration in the simulation does not increase the maximum temperature from 51.4 K, only the quantity of time the tape experiences 51.4 K. This is not the case in real life, as the energy is directly correlated to time and is synonymous with the heat transferred. The simulated boundary between the fridge at 20 K and the tape is likely making the value artificially low. Lastly, the entire bridged area experiences the same maximum temperature during this simulated pulse, supporting the assumption that the bridged area can be treated as a single thermal mass.

4.3.3 High speed thermal camera

We conducted preliminary measurements of an *ex situ* room temperature pulse with a high speed thermal camera (640 × 512 Indium Antimonide Mid-Wave Infrared Camera). We recorded infrared photons between 3 μm and 5 μm at the peak, which places the maximum temperature between 362 K and 966 K [65]. The results displayed a real time temperature profile of the HTS tape's surface consistent with the thermocouple measurements. The thermal camera is not currently compatible with the vacuum chamber because it requires thermal mirrors with a line sight onto the bridge. Furthermore, the thermal camera only measures above room temperature. This makes calibrations difficult because, even if the HTS tape's surface surpasses room temperature during a pulse, it rests at cryogenics before and after each pulse. Because of these obstacles, this thesis pursued thermocouple measurements instead of the high speed thermal camera *in situ*.

4.4 Procedure

4.4.1 Mounting and pump down

Initially, the HTS tape must be cleaned with organic solvent and placed on the sample holder with vacuum grease (although, the grease cannot touch the bridge). The sand-

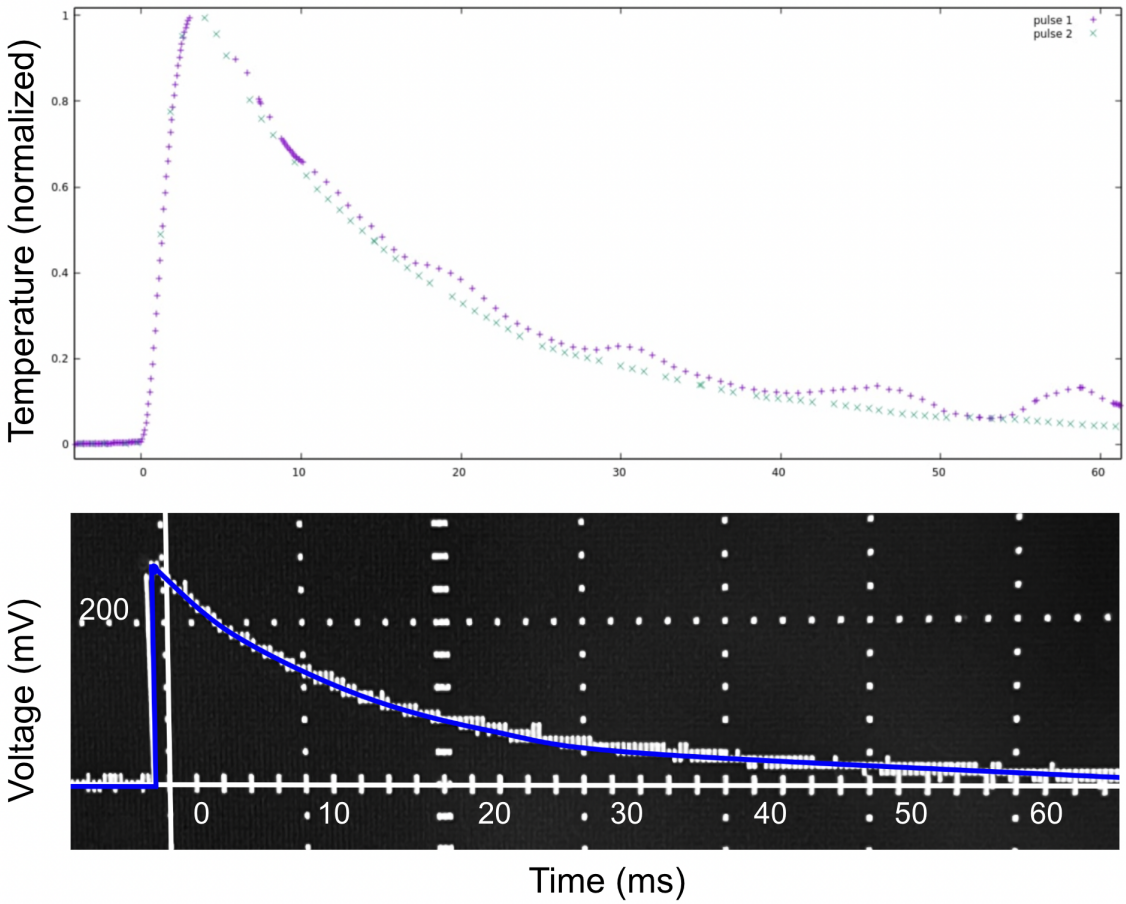

Figure 4-9: The capacitor, charged to 5 V, discharging entirely at 400 A over an unbridged HTS tape. Because we could not calibrate the thermal camera, we do not know the maximum temperature during this pulse. Still, note that the relative temperature read by the thermal camera (top) matches the oscilloscope's reading of the pulse (bottom) almost exactly.

wich top then presses the sample and thermocouple, which is surrounded by a 25 μm layer of Kapton, onto the HTS tape. This is then mounted onto the cryohead inside the vacuum chamber, which is pumped down until the chamber is approximately 5×10^{-6} Torr and 20 K.

4.4.2 Irradiation

Once the chamber's environment has a low enough pressure and temperature, a measurement of the critical current is obtained. This will function as the control critical current to monitor the amount of radiation damage the HTS tape sustains. Then,

the proton beam is created in HECTOR and shaped on the Faraday cup. When we are ready to begin irradiation, the Faraday cup is lifted. The HTS tape's critical current is measured every 5 minutes, but the Faraday cup must be closed for each of these data points (and reopened afterwards). Once the tape is at the desired level of damage (when its critical current is below 10% of its original value), HECTOR is shut off.

4.4.3 Applying pulses

Figure 4-10: The pulse box's control panel. The black on/off switch connects and disconnects the box from the circuit, the silver 1/0/2 switch controls the capacitor's ability to charge and discharge, and the voltmeter reads the capacitor's voltage.

After the irradiation is complete, the pulse box is connected to the vacuum chamber. The pulse box has two switches: one that controls the charging/discharging of the capacitor (0 for neutral, 1 for charging, and 2 for discharging), and one that connects the entire pulse box to the HTS tape (ON or OFF).

In order to apply a pulse, we first confirm that the circuit is disconnected (OFF), and then charge the capacitor with the appropriate voltage (switch position 1 and select a voltage on the variable power source). The voltmeter on the side of the box will read the capacitor's voltage. Next, we set the capacitor to neutral (switch position 0) and connect the pulse box to the HTS tape (ON). In order for the oscilloscope to acquire the pulse when the waveform generator sends the desired pulse, it must be on "Trigger" and "Ready." Between each pulse, the capacitor should be discharged (switch position 2) and the pulse box disconnected from the HTS sample (OFF).

After each pulse, we obtain the new, expectantly improved critical current. Again, it is essential that the pulse box is on OFF during the critical current measurement. This process is repeated for each current pulse.

Chapter 5

Results

5.1 First trial

During the first trial, we bombarded the sample with 1.4×10^{-3} C over approximately two hours at a current of approximately 1400 nA. This translates to a fluence of 1.3×10^{15} $\frac{\text{particles}}{\text{cm}^2}$. During irradiation, we measured the critical current with the beam line off every ten minutes to monitor the degradation of the HTS tape. When the sample's critical current reached 7% of its pristine value, we stopped the irradiation. We delivered current pulses at 400 A with durations of $10, 20$ and $30\,\mu$s without observing any noticeable changes in the critical current. The critical current increased by 23% when given a $40\,\mu$s pulse; critical current recovery is given with respect to the post-irradiation values. Two repeated pulses at $40\,\mu$s did not alter the tape's critical current. Next, we increased the pulse length to $80\,\mu$s and noticed a very slight recovery in the critical current (now at 26% recovery). The following pulse at $160\,\mu$s also resulted in a noticeable, but mild, increase in critical current (30%).

Next, we increased the length to $320\,\mu$s. The critical current seemed to jump in recovery, displaying a value 55% above the post-irradiation value. Because of the dramatic recovery in the HTS tape, we repeated this pulse three more times. The tape saw minimal change, but increased to 61% recovery. The following pulse was at $640\,\mu$s (which corresponds to 90 K) and saw the tape to 66% recovery, the highest critical current value achieved during this run.

Instead of running the next pulse at 1 ms as planned, it lasted 10 ms, burning the sample and ending the trial. This would have brought the sample to a calculated 1100 K in the tape. This experimental run occurred using version one of the sample holder and therefore did not have accurate temperature measurements. It did, however, inform us that defect annealing via current pulses is indeed possible, and that it is possible at 400 A [66].

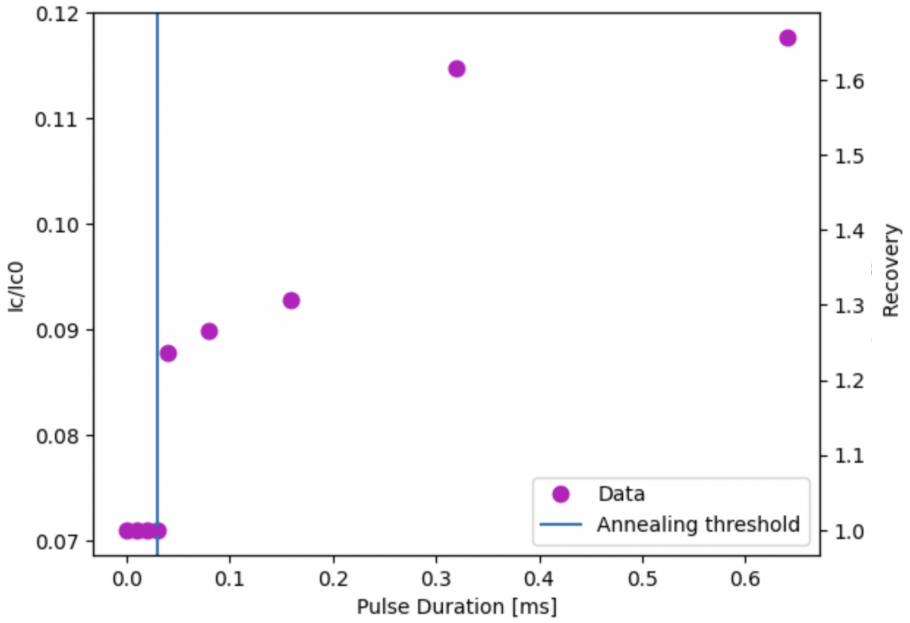

Figure 5-1: Trial one's percent recovery and normalized critical current as a function of pulse duration. This trial revealed that there is a threshold below which the tape does not reach a high enough temperature for a long enough period of time to experience annealing between 30 and 40 μs. The burn pulse is not graphed for the sake of scale.

5.2 Second trial

The second trial of this experiment's irradiation ran until the sample's critical current was only 5% of its pristine value. It required bombarding the sample with a fluence 5.4×10^{-4} C of protons, or 4.8×10^{14} $\frac{\text{particles}}{\text{cm}^2}$. The current was approximately 450 nA.

Again, all the current pulses took place at 400 A, but this time the time steps were much more methodically intervalled. They began at 0.5 ms and increased at intervals of 0.5 ms until the sample burned at 6 ms. At 3 ms, we repeated the pulse five times,

noting a slight recovery each time until a maximum amount of recovery was reached. Repeated pulsing appeared to increase the critical current much more slowly than the first pulse at each respective duration. Overall, the HTS tape's critical current underwent a steady recovery until it burned, with the maximum value at 400% that of the irradiated sample. This run identified the maximum length of a current pulse at 400 A to be between 5.5 ms (630 K) and 6 ms (680 K). Lastly, this experiment also used version one of the sample holder and therefore cannot rely on the thermocouple for the measured temperature [67].

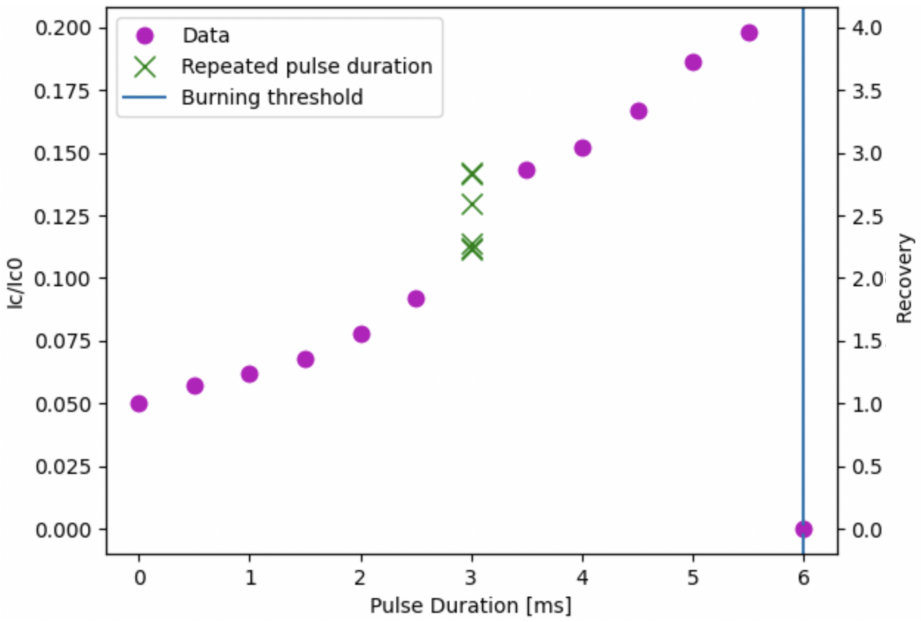

Figure 5-2: Trial two's percent recovery and normalized critical current as a function of pulse duration. This trial revealed that the threshold beyond which the HTS tape experiences too high a temperature and burns is between 5.5 and 6 ms. Furthermore, it displays a maximum amount of annealing at a given temperature.

5.3 Analysis

At 400 A, the optimal pulse length for sample recovery (up to 400%) is 5.5 ms. According to thermodynamic calculations, this corresponds to a temperature of 630 K. This temperature is clearly enough to anneal out defects in the REBCO micro structure, although we cannot yet determine which defects this process targets.

5.3.1 Uncontrolled variables

A series of parameters in this thesis may contribute to inaccuracies in the data and opportunities for better iterations of these experiments later. Most notably, the estimated temperature of the REBCO layer relies heavily on thermodynamic calculations and modelling. The sample holder was changed part way through this thesis, however all trials with version two of the sample holder failed due to miscalibrated critical current measurements. The gradation in version one of the sample holder's temperature may have increased or decreased the ambient temperature of the HTS tape by an uncontrolled amount. Furthermore, the pulse box's wires were also changed between each trial (although they are now permanently fixed).

Potentially the largest loose end is that this experiment never tests how an irradiated HTS tape reacts to a 5.5 ms pulse without being annealed via smaller pulses first. It is possible that the tape must be annealed in steps to avoid burning due to too much energy too quickly. However, we never delivered this pulse to an unannealed tape because each experimental run was too valuable to risk immediately burning the tape.

5.3.2 Next steps

This thesis has opened the door to resistive heating-based annealing in HTS tapes. The next logical step for this experiment is to identify the optimal amplitude for current pulses. Moreover, the majority of this thesis was spent building an adjustable experimental setup for testing current pulses, so increasing the quantity of trials in the future should be exponentially easier. Ideally, enough data will be collected to make an informed hypothesis as to specifically which defects in the REBCO microstructure are being annealed.

The temperature measurements in this thesis can also be improved upon. We will move the thermocouple onto the bridge for more accurate temperature measurements. In order to shelter the thermocouple from radiation, we will cover it in many layers of Kapton. The COMSOL simulation that reveals the temperature in the REBCO

layer given the temperature on the surface of the Kapton can be improved with more accurate values regarding the thermal connectivity between the tape and the sample holder. Another option includes further exploring the high speed infrared camera by installing mirrors in the chamber. Calibrating the temperature reached inside the tape at 77 K *ex situ* and then applying this knowledge to an *in situ* experiment at the same temperature is not a viable solution because the thermal camera will pick up interference from the liquid nitrogen used to cool the sample.

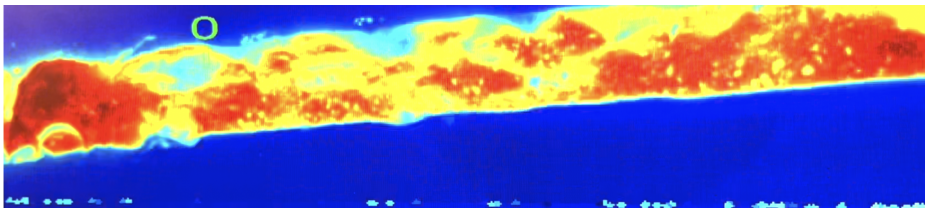

Figure 5-3: The thermal camera's view of liquid nitrogen bubbling off of an unbridged HTS sample while the capacitor discharges 5 V at 400 A.

We also hope to confirm the lack of oxygen migration in the REBCO microstructure with x-ray photoelectron spectroscopy (XPS), which measures the binding states of each type of atom nanometers into the surface of a material. By using XPS on an exposed REBCO sample, we can confirm whether the copper and oxygen remain bonded after a pulsing run (this trial will have to be careful not to reach an inevitable burn).

Although this thesis focuses on parameterizing how to best anneal out defects using a single current pulse, a brief experiment with repeated square wave pulsing would offer extensive insight. This would see if ongoing exposure to heating power continuously increases the critical current, or if a ceiling exists for each current amplitude or length (and therefore each temperature reached in the REBCO layer). In order to prevent the HTS tape from burning, a continuous current should not be used. Similarly, the pulses will occur far enough apart for the tape to completely cool between each one if they have a duty cycle of 50%. In order to match the existing experiments, this should be done with 400 A. The pulse duration may very, but should be at a duration that has already displayed recovery, such as 1 ms.

Finally, this experiment was conducted with the hope that current pulse annealing

could be used in a commercial fusion reactor one day. However, sending a current pulse all-the-way around a toroidal field coil would result in large amounts of induction. In order for annealing via fast current pulses to be a practical solution inside fusion reactors, we must first identify a distribution of current leads that appropriately minimizes induction.

Chapter 6

Conclusion

This thesis proves that fast, high amplitude current pulses can heal radiation defects in HTS tapes, a discovery with promising implications for extending tokamak lifetimes. By testing varying pulse durations at 400 A, we found that the optimal recovery, a 400% increase from the damaged tape, can be obtained via 5.5 ms pulses. Thermodynamic analysis informs us that the REBCO layer likely reaches a temperature of 630 K during these pulses.

The goal of this experiment was to display ohmic heating based annealing in irradiated HTS tapes. In order to do so, we built a experimental setup to apply controlled current pulses at varying amperage (up to 2000 A) and durations (as low as 100 ns). While this thesis only characterized recovery in 400 A pulses, it both encourages and immediately enables experimentation with varying current pulses. Furthermore, it offers a thermodynamic analysis of the HTS tape during pulsing applicable to any future resistive heating-based HTS projects.

This new mode of HTS annealing opens the door to fascinating information regarding the behavior of REBCO. Understanding that we can indeed heal HTS internally is only the beginning of what will hopefully become a robust method for increasing fusion reactor lifetimes. The study of HTS is indeed riveting, but, more importantly, it offers real world solutions issues faced in fusion energy.

Bibliography

[1] Dennis Whyte and Zach Hartwig. SPARC and the high-field strategy to fusion energy. Massachusetts Institute of Technology. `https://www.burningplasma.org/resources/ref/Web_Seminars/SPARC_seminar_USBPO.pdf`, 2018. Accessed: 2023/04/21.

[2] Zach Hartwig and Dennis Whyte. 22.061 fusion energy and plasma physics: Introduction to fusion energy. Massachusetts Institute of Technology, 2020.

[3] G. Blatter, M. V. Feigel'man, V. B. Geshkenbein, A. I. Larkin, and V. M. Vinokur. Vortices in high-temperature superconductors. *Reviews of Modern Physics*, 66:1125–1388, 10 1994.

[4] Y. Iwasa. *Case Studies in Superconducting Magnets*, page 9. Plenum Press, New York NY, 1994. ISBN: 9780387098005.

[5] D. Fischer, D Whyte, A. Devitre, K. Woller, L.A. Kesler, B Sorbom, and Z. Hartwig. HTS radiation damage under high fluence. Zoom meeting, 2019.

[6] David Fischer, Alexis Devitre, Kevin Woller, Lauryn Kortman, Zoe Fisher, and Dennis Whyte. LIFT 1 results. Zoom meeting, 2021.

[7] Lucio Rossi and Carmine Senatore. HTS accelerator magnet and conductor development in europe. *Instruments*, 5:8, 02 2021.

[8] Brandon Nils Sorbom. *The Effect of Irradiation Temperature on REBCO J_c Degradation and Implications for Fusion Magnets*. PhD thesis, Massachusetts Institute of Technology, Cambridge MA, 2017.

[9] Z.S. Hartwig. The CLASS 1.7 MV tandem ion accelerator. `http://cstar.mit.edu/tandetron.php`, 2015. Accessed: 2023/04/11.

[10] Steven Jepeal, Lance Snead, and Zachary Hartwig. Intermediate energy proton irradiation: rapid, high-fidelity materials testing for fusion and fission energy systems. *Materials and Design*, 200:109445, 01 2021.

[11] Harold Salvadore Barnard. *External Proton Beam Analysis of Plasma Facing Materials for Magnetic Confinement Fusion Applications*. PhD thesis, Massachusetts Institute of Technology, Cambridge MA, 2009.

[12] David Fischer and Alexis Devitre. Effects of radiation damage at cryogenic temperatures on high-temperature superconductors for fusion magnets. Technical report, Massachusetts Institute of Technology Laboratory for Innovation in Fusion Technology, Cambridge MA, 2021.

[13] Z.L. Fisher, D.X. Fischer, M.P. Short, A. Devitre, K.B. Woller, Z.S. Hartwig, and D.G. Whyte. Poster: Annealing cryogenically irradiated high temperature superconductors with current pulses. Applied Superconductivity Conference, Honolulu HI, 10 2022.

[14] D. R. Smith and F. R. Fickett. Low-temperature properties of silver. *Journal of Research of the National Institute of Standards Technology*, 100:119–171, 04 1995.

[15] Binyi Tian, Tengyan Wang, Yuantong Ma, Yiran Meng, Yin-Shun Wang, Qingmei Shi, and Jin Dong. Fault current characteristics of parallel stainless steel and REBCO tapes and a 6 kv/400 v hts transformer. *IEEE Transactions on Applied Superconductivity*, PP:11, 03 2021.

[16] Jun Lu, Eun Sang Choi, and Haidong Zhou. Physical properties of hastelloy® c-276™ at cryogenic temperatures. *Journal of Applied Physics*, 103:064908, 2008.

[17] ESPI Metals. `https://www.espimetals.com/index.php/technical-data/194-Silver`. Accessed: 2023/05/08.

[18] X. Y. Qin, W. Zhang, L. D. Zhang, L. D. Jiang, X. J. Liu, and D. Jin. Low-temperature resistance and its temperature dependence in nanostructured silver. *Physical Review B*, 56:120–127, 10 1997.

[19] Edward Joseph Jankowski. Convective heat transfer model for determining quench recovery of high temperature superconducting YBCO in liquid nitrogen. Master's thesis, Massachusetts Institute of Technology, Cambridge MA, 2002.

[20] M. Aravind and P.C.W. Fung. Thermal parameter measurements of bulk YBCPO superconductor using PVDF transducer. *Measurement Science Technology*, 10:979–985, 11 1999.

[21] M. Roulin, A. Junod, and E. Walker. Scaling behavior of the derivatives of the specific heat of yba2cu3o6.93 at the superconducting transition up to 16 tesla. *Physica C*, 260:257–272, 1996.

[22] A. Knizhnik, G. Shter, Gideon Grader, G. Reisner, and Y. Eckstein. Interrelation of preparation conditions, morphology, chemical reactivity and homogeneity of ceramic YBCO. *Physica C-superconductivity and Its Applications - PHYSICA C*, 400:25–35, 12 2003.

[23] Haynes International. Hastelloy X alloy physical properties. `https://www.haynesintl.com/alloys/alloy-portfolio_/High-temperature-Alloys/HASTELLOY-X-alloy/physical-properties`. Accessed: 2023/05/08.

[24] National Aeronautics and Space Administration. The effects of climate change. `https://climate.nasa.gov/effects/`, 2023. Accessed: 2023/04/11.

[25] David Fischer. *Effect of neutron radiation damage on coated conductors for fusion magnets*. PhD thesis, Technische Universität Wien, Vienna Austria, 2019.

[26] D.X. Fischer, R. Prokopec, J. Emhofer, and M. Eisterer. The effect of fast neutron irradiation on the superconducting properties of REBCO coated conductors with and without artificial pinning centers. *Superconductor Science and Technology*, 31(4):044006, 03 2018.

[27] Raphael Unterrainer, David X Fischer, Alena Lorenz, and Michael Eisterer. Recovering the performance of irradiated high-temperature superconductors for use in fusion magnets. *Science Technology*, 35:04LT01, 02 2022.

[28] A. Devitre, D.X. Fischer, K.B. Woller, Z.L. Fisher, R. Unterrainer, M.P. Short, Z.S. Hartwig, and D.G. Whyte. Poster: Annealing cryogenically irradiated high temperature superconductors with current pulses. Applied Superconductivity Conference, Honolulu HI, 10 2022.

[29] L.F. Goodrich. High tc superconductor voltage-current simulator and the pulse method of measuring critical current. *Cryogenics*, 31(8):720–727, 1991.

[30] M. Greenwald, D. Whyte, P. Bonoli, Z. Hartwig, J. Irby, B. LaBombard, E. Marmar, J. Minervini, M. Takayasu, J. Terry, R. Vieira, A. White, S. Wukitch, D. Brunner, R. Mumgaard, and B. Sorbom. The high-field path to practical fusion energy. *Massachusetts Institute of Technology and Commonwealth Fusion Systems*, 2018.

[31] John Ball and Shon Mackie. Personal conversation about the Modular Adjustable Negative-Triangularity ARC, 05 2023.

[32] L. Bromberg, M. Tekula, L.A. El-Guebaly, and R. Miller. Options for the use of high temperature superconductor in tokamak fusion reactor designs. *Fusion Engineering and Design*, 54:167–180, 02 2001.

[33] Plasma Science and Fusion Center. SPARC. `https://www.psfc.mit.edu/sparc`, 2023. Accessed: 2023/04/11.

[34] Richard Feynman. Seminar on superconductivity: The schrodinger equation in a classical context. California Institute of Technology, 1962.

[35] Emilio A. Stinzianni, Harry Efstathiadis, Kathleen A. Dunn, and Pradeep Haldar. Role of temperature and duration of the crystallization anneal in the texture development of YBCO prepared by TFA-MOD. *IEEE Transactions on Applied Superconductivity*, 19(3):2877–2881, 2009.

[36] V.V. Zubko, S.M. Ryabov, S.S. Fetisov, and V.S. Vysotsky. Heat transfer simulation to liquid nitrogen from hts tapes at the overload currents. *Physics Procedia*, 67:619–624, 2015.

[37] Ernest G. Cravalho, Joseph L. Smith, John. G. Brisson, and Gareth H. McKinley. Thermal-fluids engineering: An integrated approach to thermodynamics, fluid mechanics, and heat transfer, 2005.

[38] SuperOx. *SInnovations 2G HTS wire for in-field use*, 02 2023. 04-20Ag-40H.

[39] A. Molodyk, S. Samoilenkov, A Markelov, P. Degtyarenko, S. Lee, V. Petrykin, M. Gaifullin, A. Makevich, A. Vavilov, B. Sorbom, J. Cheng, S. Garberg, L. Kesler, Z. Hartwig, S. Gavrilkin, A. Tsvetkov, T. Okada, S. Awaji, D. Abraimov, A. Francis, G. Bradford, D. Larbalestier, C. Senatore, M. Bonura, A.E. Pantoja, S.C. Wimbush, N.M. Strickland, and A. Vasiliev. Development and large volume production of extremely high current density yba2cu3o7 superconducting wires for fusion. *Scientific Reports*, 11:2084, 01 2021.

[40] Michael Short. 22.74 radiation damage and effects in nuclear materials lectures 3-4: Diffusion. Massachusetts Institute of Technology, 2022.

[41] SuperOx. Workshop on accelerator magnets in HTS: HTS development and industrialisation, Zurich Switzerland, 2014.

[42] Vladimir Bordo. Self-excitation of radio waves in the metal-insulator-metal structure doped with metal nanowires. *Journal of Applied Physics*, 133:14301, 01 2023.

[43] A.F. Mills. *Basic Heat and Mass Transfer*, pages 2–12. Prentice Hall, Upper Saddle River NJ, 2 edition, 1999. ISBN: 0996305300.

[44] Michal Chudy, R. Fuger, M. Eisterer, and H. Weber. Characterization of commercial YBCO coated conductors after neutron irradiation. *Applied Superconductivity, IEEE Transactions on*, 21:3162 – 3165, 07 2011.

[45] Michael Short. 22.74 radiation damage and effects in nuclear materials lectures 5-7: Point defect creation, damage cascades, models for damage. Massachusetts Institute of Technology, 2022.

[46] Gary Was, Zhijie Jiao, Elizabeth Getto, Kai Sun, A.M. Monterrosa, Stuart Maloy, Osman Anderoglu, B.H. Sencer, and M.J. Hackett. Emulation of reactor irradiation damage using ion beams. *Scripta Materialia*, 88:33–36, 10 2014.

[47] Michael Short. 22.74 radiation damage and effects in nuclear materials lecture 2: Radiation effects. Massachusetts Institute of Technology, 2022.

[48] Michael Short. 22.74 radiation damage and effects in nuclear materials lectures 8-9: Point defect kinetics. Massachusetts Institute of Technology, 2022.

[49] Nuclear Regulatory Commission. Control of exposure from external sources in restricted areas. https://www.nrc.gov/reading-rm/doc-collections/cfr/part020/part020-1601.html, 1991. Accessed: 2023/04/01.

[50] Leigh A. Kesler. *Development and testing of an in situ method of ion beam analysis for measuring high-Z erosion inside a tokamak using an AIMS diagnostic*. PhD thesis, Massachusetts Institute of Technology, Cambridge MA, 2019.

[51] Tandetron Accelerator Systems. *Tandetron Manual*.

[52] Hao Wu and Guo-Hua Fan. An overview of tailoring strain delocalization for strength-ductility synergy. *Progress in Materials Science*, 113:100675, 04 2020.

[53] J.D. Verhoeven. *Fundamentals of Physical Metallurgy*, page 326. Wiley, New York NY, 2 edition, 1975. ISBN: 9781111800635.

[54] David Simeone, Jean Marc Costantini, Laurence Luneville, Lionel Desgranges, Patrick Trocellier, and Philippe Garcia. Characterization of radiation damage in ceramics: Old challenge new issues? *Journal of Materials Research*, 30:1495–1515, 05 2015.

[55] Kevin Tang. Evaluation of novel laser-skived microbridges for improved characterization of REBCO superconductor. Master's thesis, Massachusetts Institute of Technology, Cambridge MA, 2023.

[56] A.E. Siegman. *Lasers*, pages 8–11. University Science Books, Sausalito CA, 1 edition, 1986. ISBN: 9781938787447.

[57] Bright Solutions. *Wedge Short Pulse Q-Switched DPSS Laser*.

[58] National Institute of Standards and Technology. Material properties: Polyimide (kapton). Technical report, U.S. Department of Commerce, Washington D.C., 2012.

[59] Handy Chandra, Spencer Allen, Shane Oberloier, Nupur Bihari, Jephias Gwamuri, and Joshua Pearce. Open-source automated mapping four-point probe. *Materials*, 10:110, 01 2017.

[60] Tempsens Instrument. Type e thermocouple. https://tempsens.com/blog/type-e-thermocouple, 2021. Accessed: 2023/04/11.

[61] National Electrostatics Corporation. *Beam Diagnostic Components*.

[62] James R. Huddle, Patrick G. Grant, Alexander R. Ludington, and Robert L. Foster. Ion beam-induced luminescence. *Nuclear Instruments and Methods in Physics Research B*, 261:475–476, 04 2007.

[63] Onsemi. *3 A Output Current, High Speed MOSFET Gate Driver Optocoupler*, 09 2022.

[64] Nicolo Riva. Personal conversation about COMSOL Multiphysics, 04 2023.

[65] National Aeronautics, Space Administration, and the California Institute of Technology. Near, mid and far infrared. https://www.icc.dur.ac.uk/~tt/Lectures/Galaxies/Images/Infrared/Regions/irregions.html, 2012. Accessed: 2023/05/16.

[66] Zoe Fisher. Trial 1 raw data. Zenodo, https://doi.org/10.5281/zenodo.7922316, 05 2023. Accessed 05/10/23.

[67] Zoe Fisher. Trail 2 raw data. Zenodo, https://doi.org/10.5281/zenodo.7922607, 05 2023. Accessed 05/10/23.